

AT 2021loi: A Bowen Fluorescence Flare with a Rebrightening Episode, Occurring in a Previously-Known AGN

LYDIA MAKRYGIANNI ¹, BENNY TRAKHTENBROT ¹, IAIR ARCAVI ^{1,2}, CLAUDIO RICCI ^{3,4}, MARCO C. LAM ¹,
ASSAF HORESH ⁵, ITAI SFARADI ⁵, K. AZALEE BOSTROEM ^{6,7}, GRIFFIN HOSSEINZADEH ⁶, D. ANDREW HOWELL ^{8,9},
CRAIG PELLEGRINO ^{8,9}, ROB FENDER,^{10,11} DAVID A. GREEN ¹², DAVID R. A. WILLIAMS ¹³ AND JOE BRIGHT ¹⁰

¹*The School of Physics and Astronomy, Tel Aviv University, Tel Aviv 69978, Israel*

²*CIFAR Azrieli Global Scholars program, CIFAR, Toronto, Canada*

³*Núcleo de Astronomía de la Facultad de Ingeniería, Universidad Diego Portales, Av. Ejército Libertador 441, Santiago, Chile*

⁴*Kavli Institute for Astronomy and Astrophysics, Peking University, Beijing 100871, People's Republic of China*

⁵*The Racah Institute of Physics, The Hebrew University of Jerusalem, Jerusalem 91904, Israel*

⁶*Steward Observatory, University of Arizona, 933 North Cherry Avenue, Tucson, AZ 85721-0065, USA*

⁷*LSSTC Catalyst Fellow*

⁸*Las Cumbres Observatory, 6740 Cortona Drive, Suite 102, Goleta, CA 93117-5575, USA*

⁹*Department of Physics, University of California, Santa Barbara, CA 93106-9530, USA*

¹⁰*Astrophysics, Department of Physics, University of Oxford, Keble Road, Oxford OX1 3RH, UK*

¹¹*Department of Astronomy, University of Cape Town, Private Bag X3, Rondebosch 7701, South Africa*

¹²*Astrophysics Group, Cavendish Laboratory, 19 J. J. Thomson Avenue, Cambridge CB3 0HE, UK*

¹³*Jodrell Bank Centre for Astrophysics, School of Physics and Astronomy, University of Manchester, Manchester M13 9PL, UK*

Submitted to ApJ

ABSTRACT

AT 2021loi is an optical-ultraviolet transient located at the center of its host galaxy. Its spectral features identify it as a member of the “Bowen Fluorescence Flare” (BFF) class. The first member of this class was considered to be related to a tidal disruption event, but enhanced accretion onto an already active supermassive black hole was suggested as an alternative explanation. AT 2021loi, having occurred in a previously-known unobscured AGN, strengthens the latter interpretation. Its light curve is similar to those of previous BFFs, showing a rebrightening approximately one year after the main peak (which was not explicitly identified, but might be the case, in all previous BFFs). An emission feature around 4680Å, seen in the pre-flare spectrum, strengthens by a factor of ~ 2 around the optical peak of the flare, and is clearly seen as a double peaked feature then, suggesting a blend of N III $\lambda 4640$ with He II $\lambda 4686$ as its origin. The appearance of O III $\lambda 3133$ and possible N III $\lambda \lambda 4097, 4103$ (blended with H δ) during the flare further support a Bowen Fluorescence classification. Here, we present ZTF, ATLAS, Keck, Las Cumbres Observatory, NEOWISE-R, *Swift* AMI and VLA observations of AT 2021loi, making it one of the best observed BFFs to date. AT 2021loi thus provides some clarity on the nature of BFFs but also further demonstrates the diversity of nuclear transients.

Keywords: Active galactic nuclei (16), Transient sources (1861), Supermassive black holes (1663)

1. INTRODUCTION

Actively accreting supermassive black holes (SMBHs), commonly referred to as active galactic nuclei (AGN), exhibit variable emission across the electromagnetic spectrum (Fahlman & Ulrych 1975; Peterson et al. 1994; Clavel et al. 1991), and over a wide range of timescales. This “normal” AGN variability is stochastic, and varies from a few percent (over weeks) up to $\sim 20\%$ (over

decades; e.g., MacLeod et al. 2012a). Various models have been proposed to explain this stochastic optical/UV variability, motivated by accretion theory and by the observed variability phenomenology. These include accretion disk instabilities, microlensing, X-ray reprocessing of disk thermal emission, and changes in the accretion rate (see, e.g., Krolik et al. 1991; Hawkins 1993; Kawaguchi et al. 1998; Pereyra et al. 2006; Dexter

& Agol 2011; Ruan et al. 2014; Caplar et al. 2017, and references therein).

Recently, more extreme optical variability has been identified in a number of AGN where the optical/UV brightness varies by a few magnitudes in relatively short timescales (\sim few months; e.g., Graham et al. 2017; Cannizzaro et al. 2020; Rumbaugh et al. 2018; Graham et al. 2020; see also Lawrence 2018 and references therein). In addition, there are AGN where the change in brightness is also associated with spectral transitions, i.e., the continuum emission becoming bluer or redder. Rarely, more significant spectral (and related classification) transitions are seen with the appearance or the disappearance of the blue continuum and/or broad line emission that is typical of persistent, broad-line (unobscured) AGN. The latter type of events is commonly referred to as changing-look AGN (e.g., LaMassa et al. 2015; MacLeod et al. 2019; Trakhtenbrot et al. 2019a; Ricci & Trakhtenbrot 2022)¹.

Among the various types of SMBH accretion events that show a large increase in optical/UV flux, Trakhtenbrot et al. (2019b) identified a new class of flares, originally consisting of a brightening event in the ULIRG F01004-2237 (Tadhunter et al. 2017), and the transients AT 2017bgt (Trakhtenbrot et al. 2019b), and OGLE17aaj (Gromadzki et al. 2019). All of these events were long lasting, unlike other SMBH related transients such as tidal disruption events (TDEs; Rees 1988; Gezari et al. 2012; Arcavi et al. 2014; Gezari 2021; van Velzen et al. 2020). During the flare, the spectra of the Trakhtenbrot et al. (2019b) class display emission lines typical of broad-line, unobscured AGN. Importantly, they also exhibit N III λ 4640 and O III λ 3133 emission lines, which are not generally seen in AGN (e.g., Vanden Berk et al. 2001) but are produced by Bowen Fluorescence (hereafter BF; Bowen 1928) in high-velocity (a few 1000s of km s^{-1}) and dense gas in the vicinity of the accreting SMBH, as proposed several decades ago by Netzer et al. (1985). Hereafter, we thus refer to this class of events as “Bowen Fluorescence Flares” or BFFs.

In the BF mechanism, He II Ly α photons can either escape, ionize neutral H or He, or be absorbed by O III at 303.693 or 303.799 Å. These ions are then de-excited through a series of transitions, producing O III optical lines at 3047, 3133, 3312, 3341, 3444, and 3760 Å as well as a prominent FUV transition at 374.436 Å. This latter transition can be re-absorbed by ground-state N III which can then produce emission lines at 4097, 4104,

4379, 4634 and 4641 Å. The presence of strong Bowen lines is thus an indicator of extreme ultraviolet (EUV, down to 100 Å) radiation, and their observed widths associate them with the broad line region (BLR). An accretion origin could explain both the Bowen lines and perhaps the optical luminosity of these events.

BF lines have been identified in other SMBH-related transients as well. Blagorodnova et al. (2017) and Leloudas et al. (2019) identified BF lines in the spectra of optical TDEs. Malyali et al. (2021) found BF lines in the peculiar nuclear transient AT 2019avd which was associated with an extreme X-ray flare. Frederick et al. (2021) found BF lines in optical transients occurring in narrow line Seyfert 1 galaxies (NLSy1s) and suggest that three of these events (AT 2019pev, AT 2019avd and AT 2019brs) are BFFs. It is currently not yet clear which properties of the SMBHs, their (variable) accretion flows, and/or their circumnuclear gas environments give rise to transient BF emission.

Here we report optical, UV, X-ray, and radio observations of AT 2021loi, a new member of the BFF class. AT 2021loi is unique as, to our knowledge, it is the only BFF so far to occur in a previously-known broad-line AGN. In addition, it presents the strongest evidence among sources of this class (to date) for a significant rebrightening, roughly one year after its main peak.

This paper is structured as follows: in Sections 2 and 3, we report the discovery and detail the observations, and in Section 4, we present the results of their analysis. In Section 5, we discuss the possible nature of AT 2021loi and we conclude in Section 6. We adopt a flat Λ CDM cosmology throughout, with $H_0 = 70 \text{ km s}^{-1} \text{ Mpc}^{-1}$, $\Omega_M = 0.3$ and $\Omega_\Lambda = 0.7$. All magnitudes are reported in the AB system (Oke 1974), and all wavelengths are in the rest frame, unless otherwise stated.

2. DISCOVERY

An optical brightening at the center of the $z = 0.083$ active galaxy WISEA J010039.62+394230.3 was discovered in Zwicky Transient Facility (ZTF) public survey data as ZTF20aanxcpf on 2021 May 7 (UT used throughout) by Munoz-Arancibia et al. (2021), using the ALeRCE broker (Förster et al. 2021). The brightening was reported with an r -band reference subtracted² discovery magnitude of 18.84 ± 0.15 , at R.A. 22:11:21.93 and Dec +39:42:30.31 (J2000).

¹ Here, we refer to changing-look events in terms of their spectral appearance in the optical regime, and not in the X-ray regime.

² Throughout the text, the term “reference” in the context of photometry or spectroscopy is used to denote the pre-flare emission from the source, which contains both the stellar light of the host and the pre-flare AGN emission.

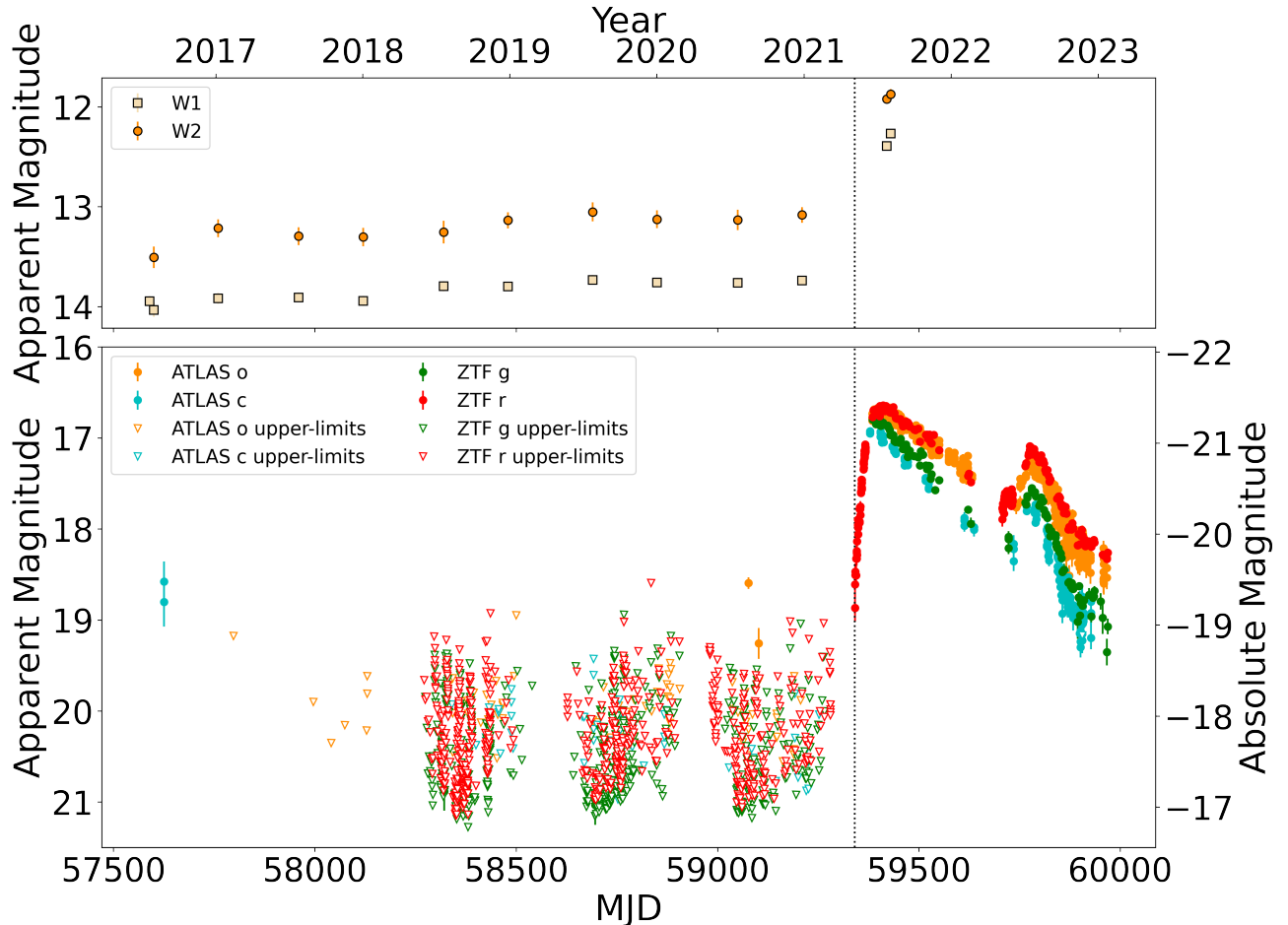


Figure 1. Top: NEOWISE-R *W1* and *W2* lightcurves (Vega magnitudes) at the position of AT 2021loi (not reference subtracted). The reference subtracted lightcurves show no significant variability prior to the optical outburst. The outburst itself is seen in both NEOWISE-R bands. Bottom: Long-term (~ 4 years) optical (ZTF *g* and *r* bands, ATLAS *c* and *o* bands) lightcurves of WISEA J010039.62+394230.3 which shows no significant variability above the non-detection 5σ upper limits. A real detection from ATLAS several years ago could correspond to a standard higher amplitude variability event of the unobscured AGN and is much lower than the recent flare. The vertical dotted line in both panels indicates the date of discovery of the optical outburst (2021 May 7, MJD 59341).

The event was classified by [Graham et al. \(2021\)](#) on 2021 June 11 (close to the optical peak at 2021 June 22) as a BFF related to enhanced accretion around an SMBH, based on a spectrum with the Low-Resolution Imaging Spectrograph (LRIS; [Oke et al. 1995](#)) on Keck I that shows broad Balmer emission lines, consistent with a narrow line Seyfert 1 (NLSy1), but also He II $\lambda 4686$, N III $\lambda 4640$ and O III 3133 and 3444 Å emission, not seen in an archival LAMOST spectrum of the source (see Sec. 3.2).

3. OBSERVATIONS

We collected follow-up observations of AT 2021loi with various facilities as detailed below.

3.1. Photometry

3.1.1. Optical, MIR and UV

We retrieved PSF-fit photometry of reference subtracted images from the ZTF forced photometry service³ from MJD = 58194 to MJD = 59975, and the Asteroid Terrestrial-impact Last Alert System (ATLAS; [Tonry et al. 2018](#)) forced photometry service⁴, from MJD = 57232 to MJD = 59975 at the position of AT 2021loi. We find no signs of strong variability in the years preceding the flare (Fig. 1).

We also obtained optical photometry in the *gri* bands, starting on 2021 July 01, with the Las Cumbres Observatory network of 1 m telescopes ([Brown et al. 2013](#)). As there are no available pre-transient Las Cumbres im-

³ <https://ztfweb.ipac.caltech.edu/cgi-bin/requestForcedPhotometry.cgi>

⁴ <https://fallingstar-data.com/forcedphot/>

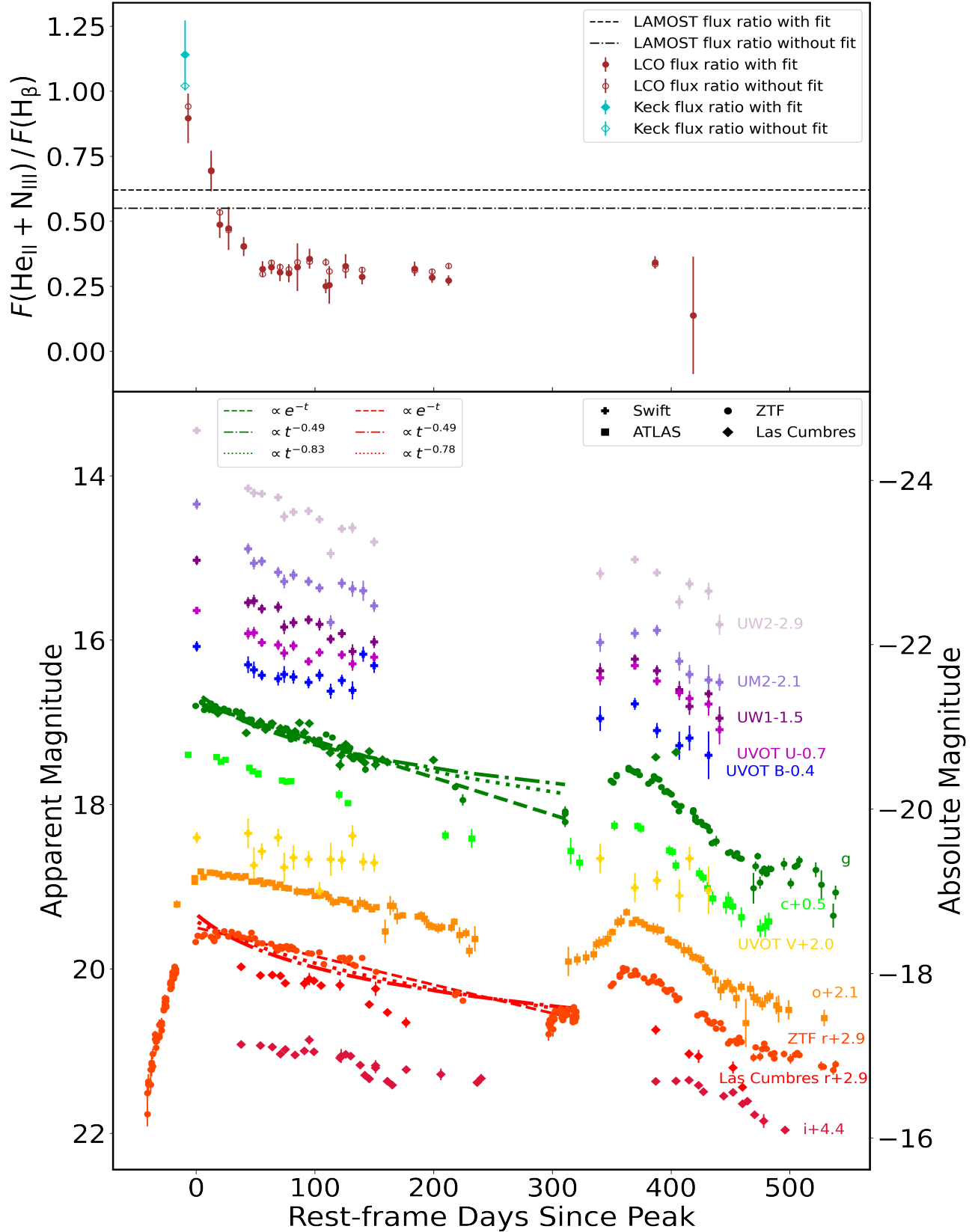


Figure 2. Bottom: Optical and UV lightcurves obtained with ZTF, ATLAS, Las Cumbres and *Swift*/UVOT. ATLAS photometry is binned in 4-day time spans. *Swift* *U*, *B* and *V* magnitudes are not reference subtracted. We present two power-law fits –one with free t_0 (dotted lines) and one with t_0 fixed to the date of discovery (dashed dotted lines), as well as an exponential fit, to the ZTF *g* and *r* band data. The best fit power-laws are shallower than the power law expected for TDEs i.e. $t^{-5/3}$. Top: the evolution of the relative flux of the spectral region that combines He II $\lambda 4686$ and N III $\lambda 4640$ to the flux of H β with and without Gaussian modeling of the emission lines.

ages of AT 2021loi, and it has yet to fade, we use Sloan Digital Sky Survey (SDSS; York et al. 2000) reference images obtained on 2006 October 6, for all three bands. We used LCOGTSNPIPE⁵ (Valenti et al. 2016) in order to process the Las Cumbres data. The pipeline is used to generate the Point Spread Function (PSF) for the Las Cumbres images and for the SDSS reference images. After that, the pipeline uses an implementation of the High Order Transform of PSF ANd Template Subtraction (HOTPANTS; Becker 2015) to perform image subtraction. We performed aperture photometry at the source position as we find that, for the Las Cumbres data, PSF-fitting produces varying residuals in the image after subtracting the PSF model. There is a noticeable difference between the ZTF and Las Cumbres r -band measurements, where the latter appears to be fainter (Figure 2). This difference is likely due to the difference in the transmission profiles of the two r filters. In Figure 3 we demonstrate this difference using an example optical spectrum of AT 2021loi along with the two r -band filter transmission functions.^{6,7} While the ZTF filter encompasses the observed broad $H\alpha$ emission line of AT 2021loi, the Las Cumbres filter does not, thus explaining why more flux is observed in ZTF r vs. Las Cumbres r .

The location of AT 2021loi was repeatedly observed in the mid-infrared (MIR) regime by the Wide-Field Infrared Survey Explorer (WISE; Wright et al. 2010) and its extensions NEOWISE (Mainzer et al. 2011) and the NEOWISE reactivation mission survey, (NEOWISE-R; Mainzer et al. 2014). The measurements were conducted in both the $W1$ and $W2$ bands (3.4 and $4.6 \mu\text{m}$, respectively). We queried the NASA/IPAC Infrared Science Archive⁸ for MIR detections within $5''$ from the ZTF-determined position of AT 2021loi. This position was visited roughly twice a year by NEOWISE-R (changes in the scanning pattern may result more observations like in this case where there are the two measurements within a few days in 2016 and 2021). We rebinned the measurements available for each such visit (using a weighted mean) into a single representative measurement per year per band. The resulting MIR lightcurve⁹ is shown in Figure 1 (top panel). Prior to the optical outburst, the MIR flux shows limited variability of

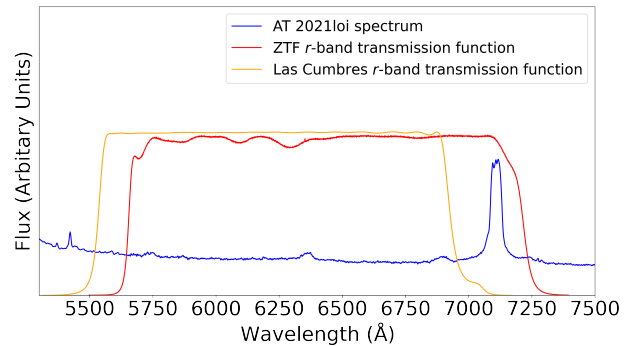


Figure 3. One of the optical spectra of AT 2021loi plotted along with the ZTF and Las Cumbres r band throughputs. The throughputs have been scaled for visualization purposes. Given the redshift of AT 2021loi ($z = 0.083$), the ZTF r -band includes the $H\alpha$ line, while the Las Cumbres one does not. This can obviously affect the corresponding flux measurements and account for the discrepancies between the corresponding lightcurves.

up to a few tenths of magnitude. The first MIR visit to show a significant flux increase (> 1.5 mag, in both MIR bands), is indeed the first measurement taken after the optical outburst, on 2021 July 22, i.e. ~ 70 days after the initial optical detection of the transient and ~ 30 days after the peak optical emission.

The earliest available WISE-based measurements associated with the the source hosting AT 2021loi (obtained through the AllWISE catalog; Cutri et al. 2021), using coadded images taken during 2010 December 11 to 2011 January 17, yield a MIR color of $W1 - W2 = 0.72$. The average MIR color during the period 2014 January 18 to 2020 December 31, probed by NEOWISE-R, i.e. the ~ 7 years prior to the optical outburst (part of it, ~ 4.5 years, is shown in Fig. 1) is $W1 - W2 = 0.66$. These MIR colors are consistent with the emission being related to an AGN, typically defined at $W1 - W2 \gtrsim 0.7$ (e.g., Stern et al. 2012; Assef et al. 2018).

We initiated near-UV (NUV) follow-up observations (PI: L. Makrygianni) with the Neil Gehrels Swift Observatory (Gehrels et al. 2004), Optical/UV Telescope (UVOT; Roming et al. 2005). We obtained twenty-three *Swift* epochs from 2021 June 21 to 2022 October 11 in all six UVOT filters ($uvw2$, $uvm2$, $uvw1$, U , B and V). UVOT photometry was extracted using the HEASARC pipeline and the standard analysis task `uvotsource`. We used a circular $7.5''$ aperture for both the source and the sky extraction regions. We use the same aperture to extract an archival NUV flux measurement from GALEX observations taken on 2006 November 09 for which we find $m_{\text{NUV}} = 20.05 \pm 0.14$ mag.

⁵ <https://github.com/LCOGT/lcogtsnpipe>

⁶ <https://lco.global/observatory/instruments/filters/>

⁷ https://github.com/ZwickyTransientFacility/ztf_information/tree/master/filter_transmission

⁸ <https://irsa.ipac.caltech.edu/frontpage/>

⁹ MIR magnitudes and colors are given in the Vega-equivalent system

Table 1. Photometry of WISEA J010039.62+394230.3.

Filter	Magnitude	Error	Source	System
<i>FUV</i>	19.86	0.21	GALEX	AB
<i>NUV</i>	20.05	0.14	GALEX	AB
<i>u</i>	18.57	0.02	SDSS	AB
<i>g</i>	17.91	0.01	SDSS	AB
<i>r</i>	17.43	0.01	SDSS	AB
<i>i</i>	17.00	0.01	SDSS	AB
<i>z</i>	16.82	0.01	SDSS	AB
<i>W1</i>	13.64	0.03	WISE	Vega
<i>W2</i>	12.92	0.03	WISE	Vega

NOTE—WISEA J010039.62+394230.3, pre-flare photometry without extinction correction applied.

Pre-flare photometry of WISEA J010039.62+394230.3 is presented in Table 1. For AT 2021loi, all photometry were corrected for Milky Way extinction using $E(B - V) = 0.045$ mag (Schlafly & Finkbeiner 2011),¹⁰ the Cardelli et al. (1989) extinction law, and $R_V = 3.1$. Our photometry is presented in Figure 1, in the bottom panel of Figure 2 and in Table 2.

3.1.2. X-ray and Radio

X-ray observations with the X-Ray Telescope (XRT; Burrows et al. 2005) on *Swift* were obtained simultaneously with the UVOT observations. Using XIMAGE to process the *Swift*/XRT images, we find no significant X-ray detection down to 3σ at the position of AT 2021loi. We then use XIMAGE to calculate the corresponding flux upper limits for each of the XRT epochs, using a circular aperture with a radius of $\sim 47''$ centered on the (optical) position of AT 2021loi (we verify that no neighboring X-ray sources are detected within that aperture). The 3σ upper limits on the X-ray flux are between 0.006 and 0.02 counts s^{-1} for the standard 0.2 – 10 keV XRT energy range. We use these to calculate the 2 – 10 keV flux upper limits, using WebPIMMS¹¹, assuming a power law photon index of $\Gamma = 1.8$, which is typical of low-redshift AGNs (e.g.; Ricci et al. 2017). The upper limits we derive are in the range $F(2 - 10 \text{ keV}) = (1.4 - 4.6) \times 10^{-13} \text{ erg cm}^{-2} \text{ s}^{-1}$. Given the source redshift, these translate to luminosity upper limits of $L(2 - 10 \text{ keV}) < (2.4 - 7.8) \times 10^{42} \text{ erg s}^{-1}$.

¹⁰ Retrieved via the NASA/IPAC Extragalactic Database (NED): <http://ned.ipac.caltech.edu/>.

¹¹ <https://heasarc.gsfc.nasa.gov/cgi-bin/Tools/w3pimms/w3pimms.pl>

Table 2. Photometry of AT 2021loi.

MJD	Filter	Magnitude	Error	Source
59341.49	<i>r</i>	18.99	0.15	ZTF
59341.49	<i>r</i>	18.73	0.14	ZTF
59342.49	<i>r</i>	18.63	0.08	ZTF
59342.49	<i>r</i>	18.59	0.09	ZTF
59344.49	<i>r</i>	18.45	0.08	ZTF
59344.49	<i>r</i>	18.63	0.11	ZTF
59345.48	<i>r</i>	18.45	0.08	ZTF
59345.49	<i>r</i>	18.36	0.08	ZTF
59345.49	<i>r</i>	18.38	0.08	ZTF
.....
59385.39	<i>r</i>	16.89	0.02	ZTF
59387.44	<i>r</i>	16.82	0.01	ZTF
59391.41	<i>r</i>	16.83	0.02	ZTF
59393.45	<i>r</i>	16.80	0.01	ZTF
59399.39	<i>r</i>	16.83	0.02	ZTF
59401.44	<i>r</i>	16.86	0.01	ZTF
59403.43	<i>r</i>	16.77	0.01	ZTF
59405.43	<i>r</i>	16.82	0.01	ZTF
.....
59428.20	<i>g</i>	17.64	0.01	Las Cumbres
59444.40	<i>g</i>	17.33	0.03	Las Cumbres
59450.10	<i>g</i>	17.24	0.02	Las Cumbres
59461.20	<i>g</i>	17.33	0.02	Las Cumbres
59469.40	<i>g</i>	17.69	0.01	Las Cumbres

NOTE—This table is published in its entirety in machine-readable format. A portion is shown here for guidance regarding its form and content.

We also initiated radio measurements with with the Arcminute Microkelvin Imager-Large Array (Zwart et al. 2008; Hickish et al. 2018, AMI-LA;) and the Karl G. Jansky Very Large Array (VLA). AMI-LA is a radio interferometer comprised of eight, 12.8 m diameter, antennas producing 28 baselines that extend from 18 m up to 110 m in length and operate with a 5 GHz bandwidth, divided into eight channels, around a central frequency of 15.5 GHz. AT 2021loi was first observed in the radio regime, at 15.5 GHz, with the AMI-LA on 2021 June 15, i.e. 39 days after optical discovery, but it was not detected. AMI-LA follow-up in the same band out to 413 days after optical discovery also resulted in non-detections. The AMI-LA observations were reduced using a customized AMI-LA data reduction software package (Perrott et al. 2013) and the 3σ flux density upper limits are in the range of 0.10 to 0.21 mJy, which correspond to radio luminosity limits of $\nu L_\nu(15.5 \text{ GHz}) < (2.6 - 5.6) \times 10^{38} \text{ erg s}^{-1}$.

We observed the field of AT 2021loi with VLA on 2021 December 1, i.e. 208 days after the initial optical detec-

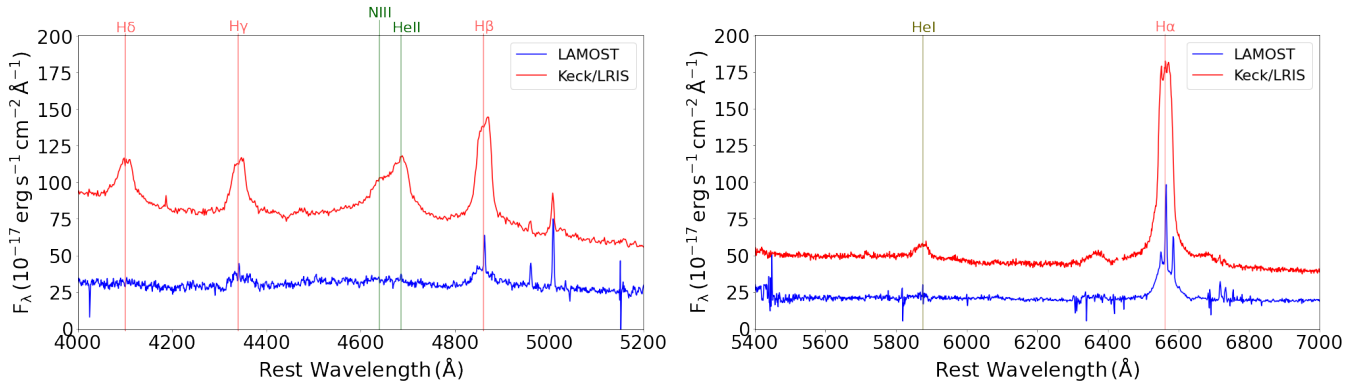


Figure 4. Comparison of the observed archival LAMOST spectrum and the raw Keck/LRIS classification spectrum. We present the regions around H β (left) and H α (right) lines. We see a clear appearance of a feature around 4680 Å in the Keck spectrum, which we interpret as BF, as well as the clear appearance of the H δ line. We also find that there is enhanced emission for HeI at ~ 5875 Å. There are also significant signs of enhanced emission at ~ 6375 Å, which corresponds to the higher ionization coronal line Fe x $\lambda 6375$.

tion. Images were produced using the CASA (McMullin et al. 2007) task CLEAN in interactive mode. While our S-band (3 GHz) image show no source above the 3σ rms limit (0.096 mJy), the C- and X-band images (5 and 10 GHz, respectively) show a source at the phase center, which we fit with the CASA task IMFIT. We estimate the peak flux density error to be a quadratic sum of the error produced by the CASA task IMFIT and an additional 10% calibration error. The flux densities at 5 GHz and 10 GHz correspond to 0.0578 ± 0.0071 and 0.0655 ± 0.0087 mJy, respectively. These, in turn, translate to radio luminosities of $\nu L_\nu(5 \text{ GHz}) = (4.9 \pm 0.6) \times 10^{37} \text{ erg s}^{-1}$ and $\nu L_\nu(10 \text{ GHz}) = (1.1 \pm 0.2) \times 10^{37} \text{ erg s}^{-1}$. Therefore, the new VLA detections correspond to a relatively weak compact radio source with a somewhat flat spectrum, and are consistent with a normal (persistent) radio-quiet AGN (e.g; Panessa et al. 2019). Given the radio data in hand and previous studies (e.g.; Smith et al. 2020 and references therein) on the correlation between radio and X-ray luminosity in AGN, we find that the radio limits and faint detections are in agreement with the upper limits for the X-ray luminosity from *Swift*.

AT2021loi is not detected in archival (NRAO¹² VLA Sky Survey; NVSS; Condon et al. 1998) radio survey data, which is complete only down to (roughly) 2.5 mJy at 1.4 GHz, and it is outside the footprint of the (slightly) more sensitive Faint Images of the Radio Sky at Twenty-Centimeters (FIRST; Becker et al. 1994) survey. Thus, we cannot say whether the new VLA detections probe an enhanced, dimmed, or persistent radio emission.

¹² National Radio Astronomy Observatory

3.2. Optical Spectroscopy

We retrieved an archival spectrum of WISEA J010039.62+394230.3, the host galaxy of AT2021loi, from the fifth data release of the Large Sky Area Multi-Object Fiber Spectroscopic Telescope survey (LAMOST/DR5; Zhao et al. 2012) obtained on 2013 December 22.¹³ The LAMOST spectrum covers the range 3500 – 9000 Å with a resolution of $R = 1800$. The archival spectrum shows AGN features, in particular prominent broad Balmer emission lines and strong narrow [O III] $\lambda 5007$.

The classification spectrum of AT2021loi (Graham et al. 2021) was obtained with the LRIS on Keck I on 2021 June 07, which covers the wavelength range between 3400 Å and 10300 Å with a resolution of $R = 600 - 1000$. This spectrum is shown in Figure 4, together with the archival LAMOST spectrum.

In addition, Figure 14 shows the two spectra normalized in a way that would yield a common integrated [O III] $\lambda 5007$ line flux level, so to further emphasize the changes in the continuum and broad line emission (see Appendix A).

We initiated a spectroscopic monitoring campaign for AT2021loi using the FLOYDS spectrograph (Sand et al. 2011) mounted on the robotic 2m telescope at Haleakalā, Hawaii (which is also part of the Las Cumbres Observatory network). During the 16 months of spectroscopic monitoring, we obtained 20 spectra. FLOYDS covers

¹³ The LAMOST archive includes a yet earlier spectrum of this source, obtained two years earlier (2011 December 28). That spectrum also shows broad Balmer emission lines, similar to the LAMOST spectrum we use. However, it is significantly affected by spectral calibration issues, including residual (sky) spectral features and uncertain spectrophotometry. We thus decided to only use the latest LAMOST spectrum.

the 3500–10000 Å range in a single exposure by capturing two spectral orders simultaneously, yielding a spectral resolution of $R \sim 400$. The exposure time of the spectra varies between 1500 and 1800 seconds and we have used a slit width of $2''$.

The Las Cumbres Observatory spectra were reduced with a custom data reduction pipeline¹⁴ built with the IRAF-free PYTHON-based ASPIRED toolkit¹⁵ (Lam et al. 2021; Lam & Smith 2022). The spectral images were each cropped into a red and a blue image. Standard data reduction procedures were applied to trace and then optimally extract the spectral information using the Horne (1986) algorithm. Wavelength calibration was performed using the built-in calibrator powered by RASCAL¹⁶ (Veitch–Michaelis & Lam 2020; Veitch–Michaelis & Lam 2021). Standard stars from the same night were used for flux calibration when available; otherwise, the ones observed closest in time to the science observations were used. Finally, atmospheric extinction and telluric absorption were removed. We present all spectra in Figure 5.

Basic details regarding all the optical spectra of AT2021loi used in this work are provided in Table 4 (in the Appendix), along with key spectral measurements (see Section 4.2).

4. ANALYSIS

4.1. Photometric Evolution

The optical brightness of AT2021loi increased by a factor of ≈ 4 between 2021 May 7 (first detection by ZTF) and 2021 June 22, from the initial $M_r = -19.04 \pm 0.15$ to peak magnitudes of $M_r = -21.08 \pm 0.03$ and $M_g = -20.98 \pm 0.04$ (all reference-subtracted). The latter corresponds to $\nu L_\nu(g) \simeq 7.8 \times 10^{43} \text{ erg s}^{-1}$. Following the peak, the optical lightcurve shows a slow, steady decline until mid-June 2022 (Figure 2). We fit the decline phase between the main peak and the re-brightening phase ($59386 < \text{MJD} < 59750$) with a power-law of the form $F \propto (t - t_0)^\alpha$. We find a power-law slope of $\alpha \simeq -0.48$ if we fix the value of t_0 to the discovery time of the optical flare, and $\alpha \simeq -0.78$ if we let t_0 (which yields $t_0 = 59253 \pm 40$) be a free parameter, with formal uncertainties of ≈ 0.01 and 0.1 , respectively. In any case, these power-laws are much shallower than the $\alpha = -5/3$ associated with TDEs (e.g.; Rees 1988), which does not provide a good fit (especially for the r band) for the data (Figure 2). After mid-June 2022, AT2021loi ex-

periences a rebrightening and shows a second peak in the ZTF r -band at $M_r = -20.59 \pm 0.05$ mag on 2022 July 15, about 390 days after the main peak. This second peak is also seen in the ZTF g and ATLAS o and c bands. An observational gap did not allow Las Cumbres gri bands to cover the rebrightening. The decline after the second peak, although faster ($\alpha \simeq -0.9$, r band), it is still very different to that of TDE.

We compare the *uvm2* UVOT observations to the archival GALEX (NUV; $\lambda_{\text{eff}} = 2304 \text{ \AA}$) data as *uvm2* ($\lambda_{\text{eff}} = 2245 \text{ \AA}$) is the most relevant UVOT filter for such a comparison. In the first UVOT observation, which also resulted in the highest NUV flux we obtained during our monitoring campaign, we measure a *uvm2* absolute magnitude of $M_{uvm2} = -21.06 \pm 0.07$ which corresponds to $\nu L_\nu(\text{NUV}) = 2.3 \times 10^{44} \text{ erg s}^{-1}$. This is a factor of ~ 20 increase from the archival GALEX detection, where the $M_{\text{NUV}} = -17.84 \pm 0.14$ magnitude translates to a $\nu L_\nu(\text{UV}) = 1.1 \times 10^{43} \text{ erg s}^{-1}$. Following this measurement, the NUV flux shows a gradual decline before the rebrightening mentioned above. The monochromatic NUV luminosity we measure ~ 14 months after the initial transient detection (and one year after the initial *Swift* detection) is $\nu L_\nu \simeq 5.7 \times 10^{43} \text{ erg s}^{-1}$, i.e., a drop of $\sim 75\%$ but still higher than the archival GALEX measurement by a factor of ~ 5 .

As already mentioned in Section 3.1.1, the MIR lightcurves (Figure 1, top panel) show limited variability prior to the optical flare, and a noticeable flux increase in the first MIR measurement that follows the optical flare. This enhanced MIR emission is separated by at most ~ 64 days from the detection of the optical outburst or ~ 30 days compared with the peak optical emission (both in the rest-frame). These timescales are mere upper limits on the real delay, driven by the (low) cadence of the NEOWISE-R monitoring. To put these timescales in context, we note that the inner edge of the dusty torus, i.e. where the temperature reaches the sublimation threshold, is expected to be $\sim 100 - 300$ light days away from the central engine, based on our near-peak L_{bol} estimate for AT2021loi. This range is driven by the range in possible dust grains (see Equations 2 & 3 in Mor et al. 2009) and is supported by NIR reverberation mapping campaigns (e.g. Suganuma et al. 2006; Koshida et al. 2014).

We can thus infer that, given the data in hand, the increase in MIR emission is broadly consistent with the reprocessing of the (sharp) rise in UV/optical radiation by circumnuclear dust, in a way that is not markedly different from what is seen in normal (persistent) AGNs. From the NEOWISE-R lightcurves, there is also some variability in the $W1 - W2$ color, which

¹⁴ https://github.com/cylammarco/FLOYDS_pipeline

¹⁵ <https://github.com/cylammarco/ASPIRED>

¹⁶ <https://github.com/jveitchmichaelis/rascal>

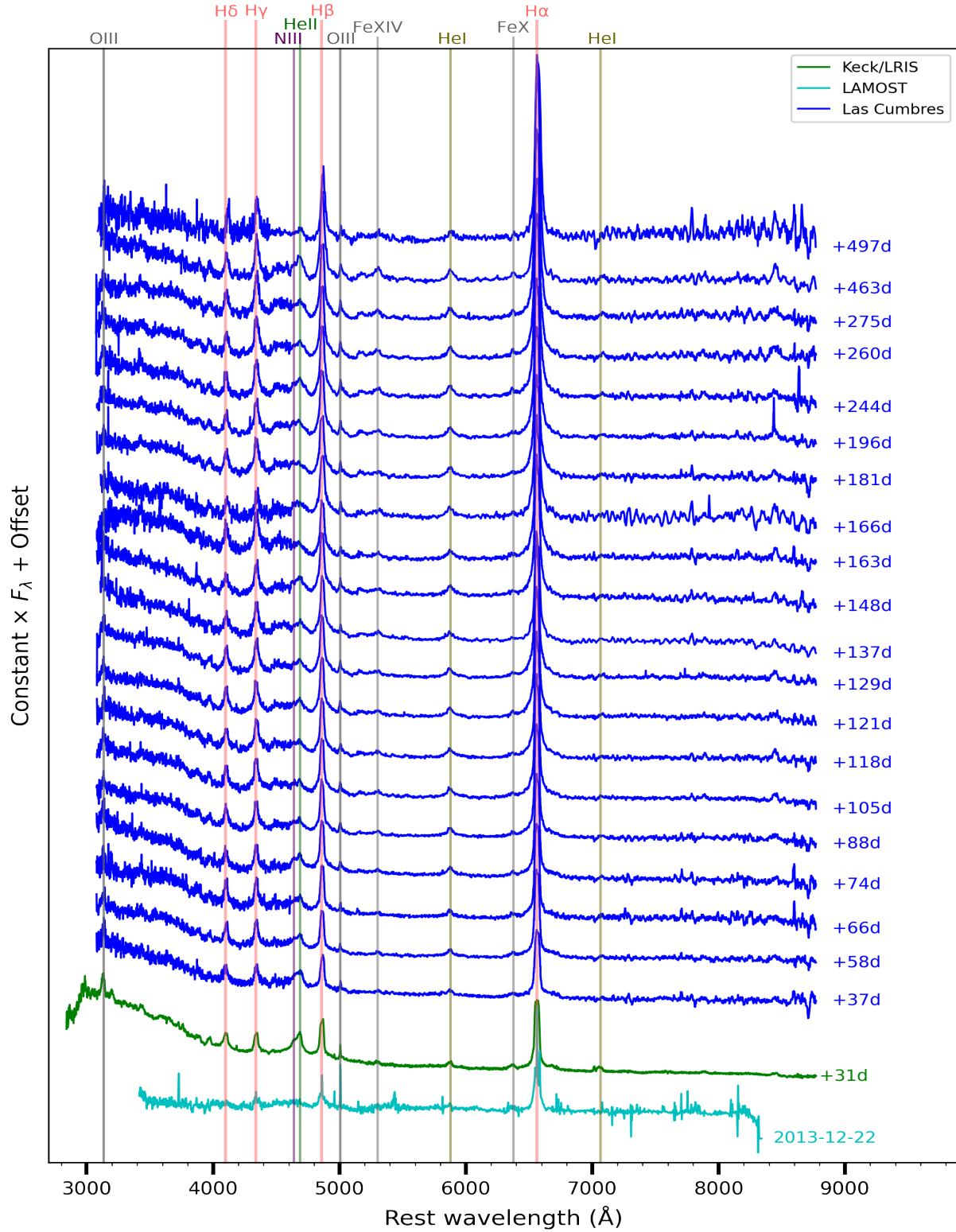


Figure 5. Spectral sequence of AT 2021loi together with the LAMOST pre-flare spectrum. Phases are noted in observed days from discovery. Persistent, for over a year, emission features include broad Balmer lines, a feature around 4680 Å as well as He I emission at 5875 Å. We also see strong, persistent O III emission at 3133 Å for at least four months after the transient detection.

changes from around 0.66 mag prior to the outburst, to ~ 0.40 mag during the transient state. While the former, pre-outburst MIR color is close to the cut used to identify AGN (i.e., $\gtrsim 0.7$), the latter post-flare color is in fact, less consistent with what is found for persistent AGNs. This may not be surprising, given the possibility that the emission from either the exceptionally UV-bright flare and/or the hottest, pure-graphite part of the torus is enhancing the shorter-wavelength *W1* band (i.e. relative to normal AGNs).

There is no ROSAT counterpart to WISEA J010039.62+394230.3 in the all-sky survey conducted during 1990–1991. From this we infer an archival 3σ X-ray upper-limit of $F(0.1–2.4\text{ keV}) \lesssim 10^{-13}\text{ erg cm}^{-2}\text{ s}^{-1}$ (Boller et al. 2016), which translates to $L(0.1–2.4\text{ keV}) \lesssim 2 \times 10^{42}\text{ erg s}^{-1}$ but also to $L(2–10\text{ keV}) \lesssim 2.5 \times 10^{42}\text{ erg s}^{-1}$. In order to compare this archival ROSAT upper limit with the post-flare XRT upper limits described in Section 3.1.2, we utilize the observed relation between X-ray and NUV emission in persistent AGNs, which is commonly quantified through the anti-correlation between the optical-to-X-ray spectral slope, $\alpha_{\text{OX}} \equiv \log(f_\nu[2\text{ keV}]/f_\nu[2500\text{ \AA}])/\log(\nu[2\text{ keV}]/\nu[2500\text{ \AA}])$, and the monochromatic NUV luminosity (see, e.g., Just et al. 2007; Lusso & Risaliti 2016; Nanni et al. 2017, and references therein).

Specifically, we rely on the relation derived in Eq. 2 of Nanni et al. (2017), of the form $\alpha_{\text{OX}} = -0.155 \log(L_{2500\text{ \AA}}) + 3.206$. From the (extinction corrected) archival GALEX NUV magnitude of AT 2021loi, $m_{\text{NUV}} = 19.65$, we derive an archival NUV luminosity of $L_\nu = 8.5 \times 10^{27}\text{ erg s}^{-1}\text{ Hz}^{-1}$. Plugging this into the Nanni et al. (2017) relation, the expected spectral slope is $\alpha_{\text{OX}} = -1.12$, which in turn yields an intrinsic monochromatic X-ray luminosity at 2 keV of $\nu L_\nu(2\text{ keV}) = 5.6 \times 10^{42}\text{ erg s}^{-1}$. Extrapolating the 2 keV fluxes to the 2–10 keV range assuming a photon index of $\Gamma = 1.8$, we derive an expected X-ray luminosity of $L(2–10\text{ keV}) \simeq 6 \times 10^{42}\text{ erg s}^{-1}$, which is a factor of ~ 3 higher than the upper limit from ROSAT. We stress that this estimate for the expected X-ray emission of AT 2021loi carries significant uncertainties. In particular, a 1σ uncertainty of ≈ 0.2 on α_{OX} at any given $L_{2500\text{ \AA}}$ (consistent with what is reported in Nanni et al. 2017) would translate to an uncertainty of almost 0.6 dex on the expected X-ray luminosity we de-

rive through this approach (i.e., a factor of ~ 4).¹⁷ Following the same approach for the near-peak *Swift* NUV measurement, of $m_{\text{NUV}} = 16.82$, yields $\alpha_{\text{OX}} \simeq -1.33$ and $L(2\text{ keV}) = 3.1 \times 10^{43}\text{ erg s}^{-1}$. Extrapolating the 2 keV flux to the 2–10 keV range using $\Gamma = 1.8$, we derive an expected X-ray luminosity of $L(2–10\text{ keV}) = 5.0 \times 10^{43}\text{ erg s}^{-1}$. The upper limits from *Swift*/XRT correspond to $L(2–10\text{ keV}) < (2.4–7.8) \times 10^{42}\text{ erg s}^{-1}$. This means that if the broad-band SED of AT 2021loi would have followed that of persistent broad-line (unobscured) AGNs, then—based on the near-peak NUV emission—the source should have been detected in the X-rays, while in practice, it was not. We discuss this further in Section 5.1.

Figure 6 shows the color evolution of the UV bright AT 2021loi compared to that of the BFF AT 2017bgt (Trakhtenbrot et al. 2019b) and the BF TDE AT 2018dyb (Leloudas et al. 2019). The color of AT 2021loi shows limited evolution similar to that of AT 2017bgt. Also, AT 2021loi is redder compared to AT 2018dyb.

We fit a blackbody to the ZTF (*g* and *r*), ATLAS (*c* and *o*), LCO (*g* and *i*) and all the *Swift* photometry for each epoch in which we have *Swift* data (linearly interpolating neighboring optical epochs), using the blackbody fitting tool SUPERBOL¹⁸ (Nicholl 2018). We then calculate the bolometric luminosity by integrating each observed SED, approximating the missing flux outside the observed bands, using the blackbody fits. Our results are presented in Figure 7. The peak blackbody temperature (i.e., at UV peak but also the peak temperature) is $(21.1 \pm 1.5) \times 10^3\text{ K}$. After ~ 43 days (in rest-frame) it declines to $(15.8 \pm 1.2) \times 10^3\text{ K}$, eventually reaching $(14.4 \pm 1.8) \times 10^3\text{ K}$. At these temperatures, we are sampling the blackbody continuum fully, especially with the UV data (Arcavi 2022).

Compared to a large compilation of TDEs (van Velzen et al. 2020), AT 2021loi is on the low-temperature end. Moreover, AT 2021loi has a steady slow decline, unlike several TDEs, which show a decline followed by a rise in temperature. In terms of inferred radius, AT 2021loi has larger blackbody radii ($1.8–2.6 \times 10^{15}\text{ cm}$) compared to the vast majority of the van Velzen et al. (2020) TDEs (typical $\lesssim 6 \times 10^{14}\text{ cm}$) and shows very little evolution. In contrast, TDE radii decline a few weeks after peak. The peak bolometric (blackbody) luminosity of

¹⁷ Other sources of uncertainty include the possible range of Γ (Ricci et al. 2017) and the fact that some AGNs are known to be “X-ray weak” (i.e. have significantly lower α_{OX} given their NUV emission; see Luo et al. 2015 and references therein).

¹⁸ <https://github.com/mnicholl/superbol>

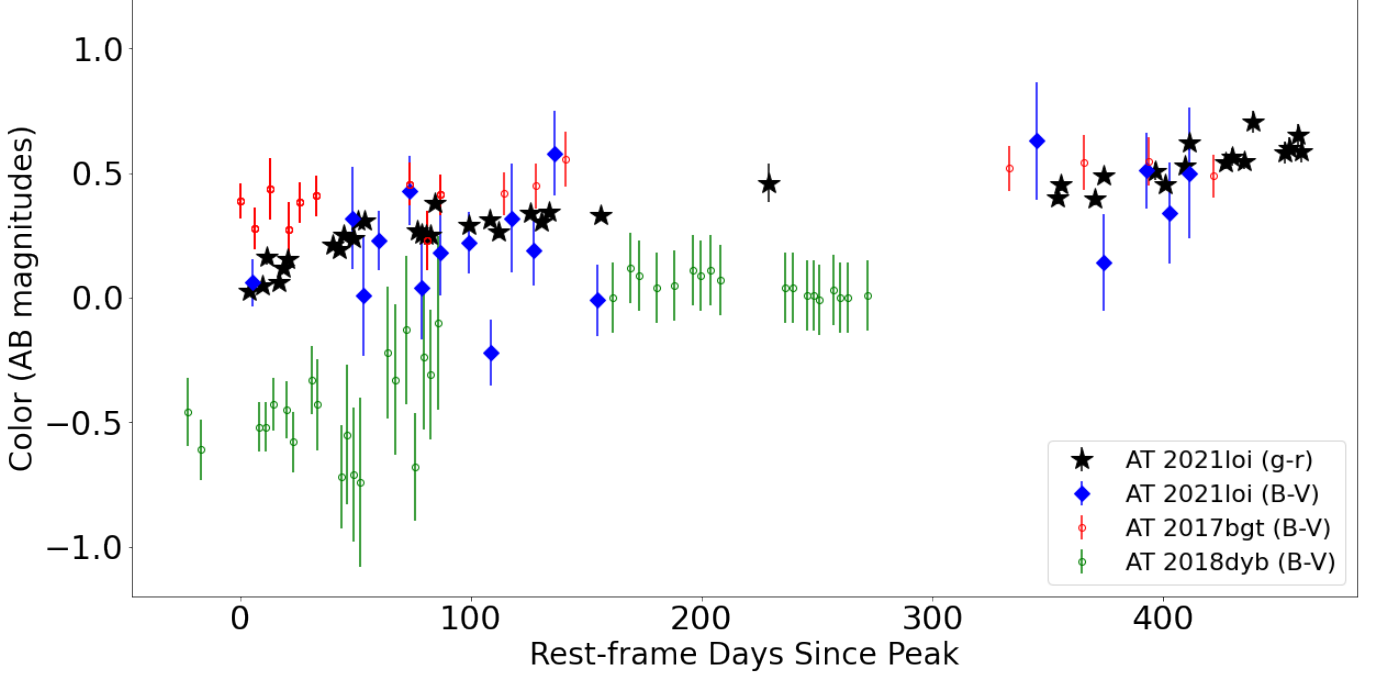


Figure 6. Color evolution ($g-r$ and $B-V$) of AT 2021loi, the BFF AT 2017bgt, and the BF TDE AT 2018dyb. AT 2021loi is redder around the peak than AT 2018dyb. AT 2021loi also shows very limited color evolution, similar to AT 2017bgt.

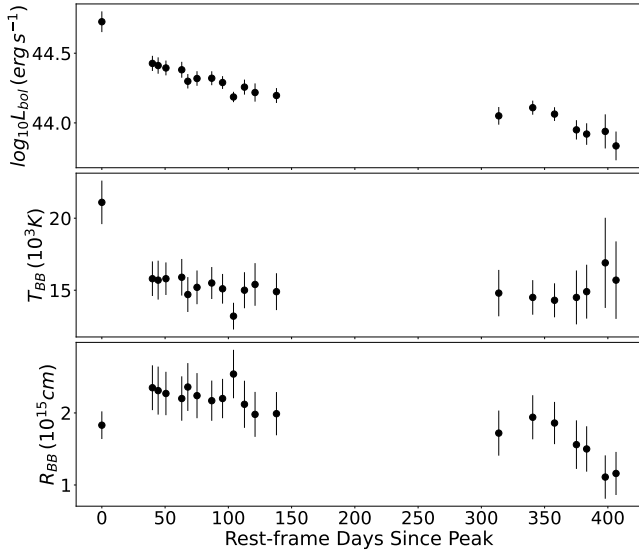


Figure 7. The bolometric luminosity (top), temperature (middle), and radius (bottom) from fitting a blackbody to the UV and optical photometry.

AT 2021loi is $L_{bol}^{BB} = 4.8 \times 10^{44}$ ergs $^{-1}$, which is higher than the majority of the TDEs presented in van Velzen et al. (2020). In comparison, the estimated temperature at the peak of the OGLE17aaj BFF is $4 \times 10^4 K$, which is much higher than that of AT 2021loi. (Gromadzki et al. 2019).

4.2. Spectroscopic Evolution

We use the PYQSOFIT fitting procedure¹⁹ (Guo et al. 2018) to model both the archival LAMOST spectrum, the first flare Keck spectrum and the FLOYDS spectra. PYQSOFIT fits and decomposes the continuum emission (with AGN and host galaxy components) and fits the broad and narrow emission lines. The continuum is fitted as a simple power law, and we add a polynomial component when fitting fails without it. All narrow emission lines are modeled with a single Gaussian, whereas the broad lines are modeled with either one or two Gaussians. We initially tried to model all broad emission lines with a single (broad) Gaussian, which works for simpler and/or weaker broad line profiles (e.g. $H\delta$). However, we found that some line profiles (e.g., $H\beta$) are more complex and two broad components are required to achieve a satisfactory fit. These multiple broad Gaussians are not constrained in terms of offset velocity, peak intensity, or any other parameter. We stress that the choice to use either one or two broad Gaussian profiles was applied consistently to all spectra (i.e., all epochs). This fitting approach is in line with common practice in fitting the (sometimes complex) broad line emission profiles in normal, persistent AGNs (see, e.g., Greene & Ho 2005; Shen et al. 2011; Trakhtenbrot & Netzer 2012a; Mejía-Restrepo et al. 2018; Rakshit et al. 2020). We fit the 4500 to 5100 Å region, which covers

¹⁹ <https://github.com/legolason/PyQSOFit>

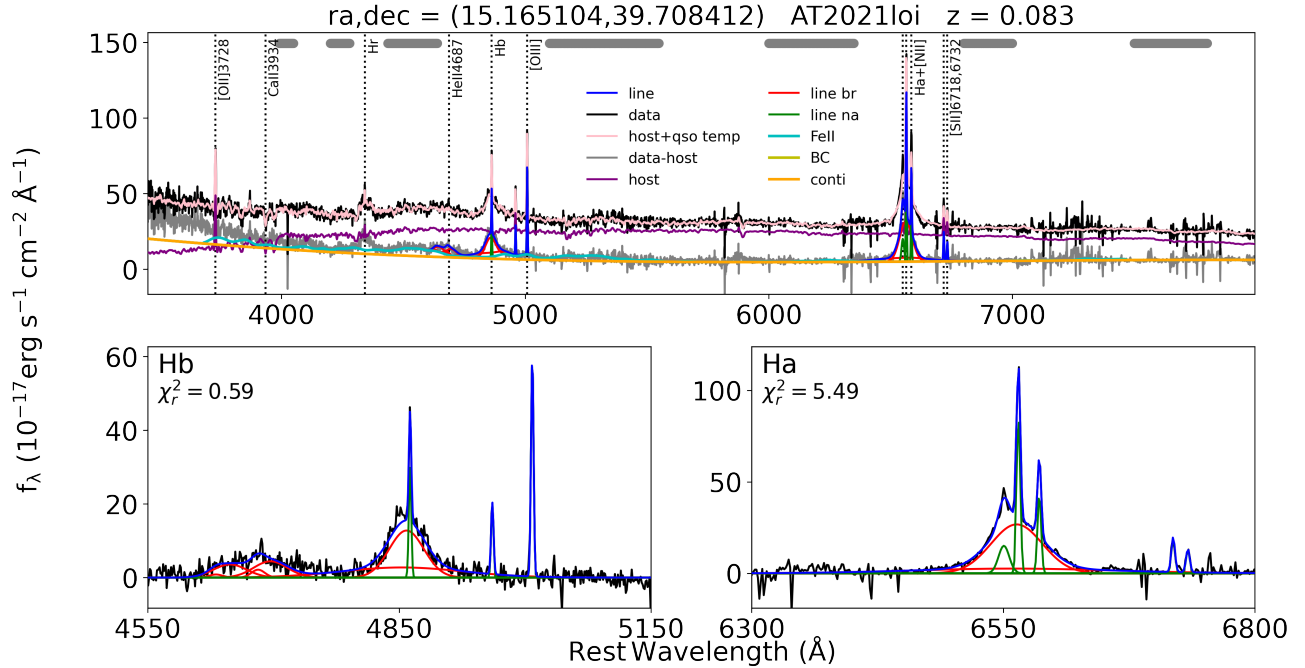


Figure 8. Decomposition of the archival LAMOST spectrum with PYQSOFIT along with the best-fit model and the model components. Gray horizontal lines on the top show the windows used for the continuum estimate. The black line represents the initial data, whereas the gray line represents the host subtracted data. The host is plotted as the purple line. The best-fit emission lines, as a sum of narrow (green line) and broad lines (red line), are marked in blue. The bottom subplots are a zoomed version of the components for H α and H β .

the entire N III $\lambda 4640$ and He II $\lambda 4686$ region as well as H β and the [O III] $\lambda\lambda 4959, 5007$ lines. In addition, we fit the H α region, including the [N II] $\lambda\lambda 6548, 6584$ and [S II] $\lambda\lambda 6718, 6732$ doublets.

We first fit the archival spectrum from LAMOST with all the available components within PYQSOFIT (i.e., the host component, the power law continuum, the Balmer continuum, and the iron emission). The fit results are presented in Figure 8. This spectrum shows broad Balmer emission lines with FWHM(H α) and FWHM(H β) $\simeq 3000 \text{ km s}^{-1}$, thus clearly capturing a broad-line, unobscured AGN. In addition, it also shows strong narrow [O III] $\lambda 5007$ emission. The key diagnostic narrow line ratios are $\log([\text{O III}] \lambda 5007/\text{H}\beta) \simeq 0.31$ and $\log([\text{N II}] \lambda 6583/\text{H}\alpha) \simeq -0.30$, which would correspond to the composite region in the BPT (Baldwin et al. 1981) - i.e. both star formation and AGN activity are responsible for producing the narrow lines in this galaxy (Kewley et al. 2006). Table 4 (in the Appendix) lists some key spectral measurements resulting from our analysis.

Based on relations between luminosity and broad line region (BLR) size derived from reverberation mapping campaigns, the LAMOST spectrum yields a BLR size of $R_{\text{BLR}} \simeq 2.9$ and 5.4 light days using the prescriptions of Trakhtenbrot & Netzer (2012b) and Bentz et al.

(2013) respectively. We use the $L(\text{H}\alpha)$ luminosity and the respective FWHM(H α) to calculate the SMBH mass following Equation 2 in Mejía-Restrepo et al. (2022) and find $M_{\text{BH}} = 1.0 \times 10^7 M_{\odot}$. The uncertainties of such mass estimates are of the order 0.3-0.5 dex, including uncertainties on both the $R_{\text{BLR}} - L_{5100}$ relation and the so-called virial factor (see, e.g., Shen 2013; Mejía-Restrepo et al. 2022, and references therein). We estimate the bolometric luminosity (L_{bol}) from the host galaxy subtracted monochromatic luminosity at rest-frame 5100 \AA ($3.2 \times 10^{42} \text{ erg s}^{-1}$) and a bolometric correction of $f_{\text{bol}}(5100 \text{ \AA}) \equiv L_{\text{bol}}/L_{5100} = 9.26$ (e.g., Shen et al. 2008; MacLeod et al. 2010). This estimate has an uncertainty of order ~ 0.3 dex, due to the uncertainty on the bolometric correction (e.g., Runnoe et al. 2012; Duras et al. 2020, and references therein). From L_{bol} and M_{BH} , we derive an estimate for the pre-flare Eddington ratio of $L/L_{\text{Edd}} \approx 0.02$ (with large systematic uncertainties, stemming from both L_{bol} and M_{BH}). Despite the large uncertainties associated with this Eddington ratio estimate, we conclude that the source, in its pre-flare state, was well within the sub-Eddington accretion regime.

The earliest spectrum after the flare, which is also the one nearest the optical peak time, is the Keck/LRIS spectrum obtained 31 days after discovery. Since the

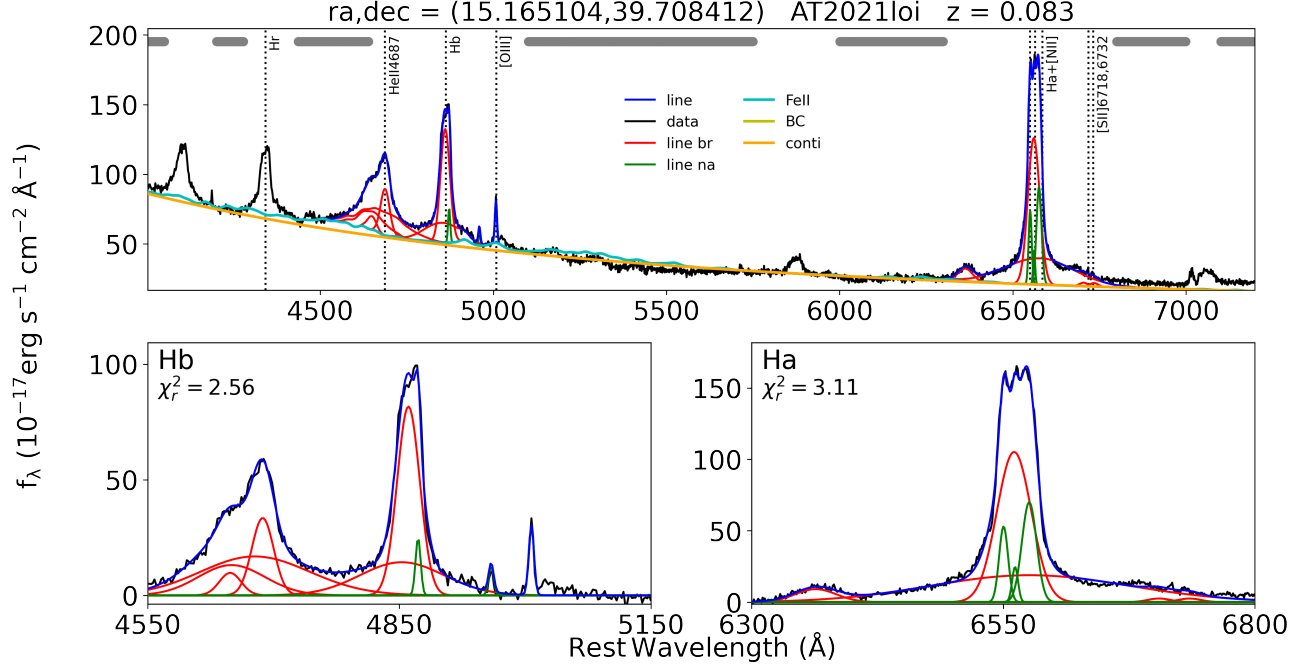


Figure 9. Decomposition of the Keck spectrum with PYQSOFIT along with the best-fit model and the model components. Grey horizontal lines on the top show the windows used for the continuum estimate. The black line represents the host subtracted data. The best-fit emission lines, as a sum of narrow (green line) and broad lines (red line), are marked in blue. The bottom subplots are a zoomed version of the components for H α and H β .

Keck spectrum has a lower resolution compared to LAMOST, we use the host component as measured for the LAMOST spectrum by PYQSOFIT to apply host subtraction to the Keck spectrum. After that, we process the Keck spectrum with PYQSOFIT (Figure 9) without applying host decomposition but only continuum fitting, iron fitting, and emission lines fitting.

For the Keck spectrum, we find $L_{5100} = 3.0 \times 10^{43} \text{ erg s}^{-1}$. From this, along with the M_{BH} estimated from the LAMOST spectrum and the same bolometric correction as mentioned above, we derive an Eddington ratio at the epoch of the Keck spectrum (i.e. near-peak) of $L/L_{\text{Edd}} \approx 0.2$. This is an increase by a factor of ~ 10 compared to the pre-flare phase, but it is still well within the sub-Eddington regime. The UV peak luminosity found in section 4.1, combined with a UV bolometric correction of $f_{\text{bol}}(\text{UV}) = 3.5$ (see Kaspi et al. 2000; Netzer et al. 2016), yields a bolometric luminosity of $7.7 \times 10^{44} \text{ erg s}^{-1}$, which in turn gives $L/L_{\text{Edd}} \simeq 0.5$. The higher value of UV-based L_{bol} estimate is a result of the UV-bright nature of the transient. Although more than twice higher than what is found from L_{5100} , the UV-based L/L_{Edd} estimate is still within the sub-Eddington regime, although we note that the large systematic uncertainty on this estimate means it is formally consistent with $L/L_{\text{Edd}} \approx 1$. The bolometric luminosity generated from the blackbody fit in the previous sec-

tion is $4.8 \times 10^{44} \text{ erg s}^{-1}$, which is lower than the one estimated from the UV flux, resulting in an even lower Eddington ratio. In any case, notwithstanding the range of L/L_{Edd} estimates and the significant systematic uncertainties associated with them, we can still conclude that the data in hand does not support a scenario in which the AT 2021loi flare approached the Eddington limit of the accreting SMBH.

In Figure 10, we plot the LAMOST and Keck spectra divided by the power-law continuum and the iron component as fitted by PYQSOFIT in order to see the difference in the strength of the emission lines with respect to the continuum and iron complex. We see that the relative strength of the feature around 4680 Å to H β has increased. In order to quantify the changes in the He II $\lambda 4686$ +N III $\lambda 4640$ region between the LAMOST pre-flare and Keck (near optical peak) spectra, we perform the following procedure on both spectra. We start by fitting both the He II $\lambda 4686$ and N III $\lambda 4640$ complex with two Gaussian components for each transition, forcing the widths to match that of the H β broad component. Each of these broad components is allowed to have a FWHM in the range of 2000 – 10000 km s^{-1} . In the case of LAMOST, although it is possible to fit the emission feature around 4680 Å (FWHM > 6000 km s^{-1}) as either one or two components (i.e. only He II $\lambda 4686$ or He II $\lambda 4686$ blended with N III $\lambda 4640$), it is not clear if

the feature indeed consists of two peaks. In the case of the Keck spectrum, we see two peaks more clearly, similar to previously identified BFFs. We list the flux (measured with PYQSOFIT) ratios between emission lines of interest in Table 3.

We look for differences in the integrated flux density of the total He II $\lambda 4686$ and N III $\lambda 4640$ region relative to the integrated flux density of H β . We do this by integrating the flux density after host, continuum, and iron subtraction between 4580 Å and 4750 Å (the region that covers He II $\lambda 4686$ and N III $\lambda 4640$) and between 4800 Å and 4900 Å (the region that covers H β). We use two approaches to quantify this ratio. In the first case, we integrate the observed flux in the region with no emission line fitting. We find that the ratio between the integrated fluxes in the two regions is 0.53 for the LAMOST spectrum and 1.12 for the Keck spectrum, meaning that the ratio increased by a factor of ≈ 2 . Using the flux as extracted from the Gaussians fit to the emission lines, we find a similar line ratio increase from $F(\text{He II } \lambda 4686 + \text{N III } \lambda 4640)/F(\text{H}\beta) \sim 0.58$ in the LAMOST spectrum to $F(\text{He II } \lambda 4686 + \text{N III } \lambda 4640)/F(\text{H}\beta) \sim 1.09$ in the Keck spectrum.

We also find that the ratio between the integrated flux without fitting the H δ spectral region (4050–4150 Å) to that of H β increased from 0.22 ± 0.01 in the LAMOST spectrum to 0.35 ± 0.02 in the Keck spectrum. The flux ratio of $F(\text{H}\delta)/F(\text{H}\beta)$ from Gaussian fitting increased from 0.24 ± 0.02 in the LAMOST spectrum to 0.36 ± 0.03 in the Keck one. On the other hand, the flux ratio of H γ to H β remained consistent with $F(\text{H}\gamma)/F(\text{H}\beta) = 0.51 \pm 0.02$ for LAMOST and 0.48 ± 0.03 for Keck (without fitting) and at $F(\text{H}\gamma)/F(\text{H}\beta) = 0.48 \pm 0.05$ for LAMOST and 0.41 ± 0.03 for Keck (with fitting). We find, though, that the $F(\text{H}\gamma)/F(\text{H}\beta)$ ratio remained constant, whereas the $F(\text{H}\delta)/F(\text{H}\beta)$ significantly increased by ~ 1.5 , providing more support for the BF mechanism as the H δ feature is likely blended with N III emission at $\lambda\lambda 4097, 4104$ (Netzer et al. 1985).

Although the spectrum appears to have a strong iron bump around 4500–4600 Å after the PYQSOFIT fitting, we find that He II at 4687 Å was present in the archival LAMOST spectrum. Typically, in AGN, $F(\text{He II } \lambda 4686)/F(\text{H}\beta) \leq 0.05$ (Vanden Berk et al. 2001). For the LAMOST spectrum, the intensity ratio $F(\text{He II } \lambda 4686 + \text{N III } \lambda 4640)/F(\text{H}\beta)$ is ~ 0.5 , which is already 10 times higher than typical AGN. For the Keck spectrum where N III $\lambda 4640$ and He II $\lambda 4686$ lines can be clearly separated, we find that $F(\text{He II } \lambda 4686)/F(\text{H}\beta) = 0.71 \pm 0.09$, $F(\text{N III } \lambda 4640)/F(\text{H}\beta) = 0.47 \pm 0.07$ and $F(\text{N III } \lambda 4640)/F(\text{He II } \lambda 4686) = 0.66 \pm 0.11$. Given the $F(\text{He II } \lambda 4686)/F(\text{H}\beta)$ and $F(\text{N III } \lambda 4640)/F(\text{H}\beta)$ ratios

seen in AT2021loi and the predicted relative intensities for AGN as suggested by Netzer et al. (1985), the gas producing the BF must have a very high density ($n_H > 10^{9.5} \text{ cm}^{-3}$) and higher N and O abundances relative to the cosmic ones. We find that the [He I] $\lambda 5875$ flux relative to [O III] $\lambda 5007$ increased from 1.17 in the LAMOST spectrum to 2.53 in the Keck spectrum; however, the flux ratio to H β has decreased from 0.27 in the LAMOST to 0.13 in Keck.

To trace the evolution of the key spectral features of AT2021loi, we apply the PYQSOFIT fitting also to the lower resolution Las Cumbres/FLOYDS spectra, using the same approach as we did for the Keck spectrum (i.e., subtracting the host component as extracted from the archival LAMOST spectrum). We use the same two approaches as before, i.e., first integrating over the observed flux in the region with no emission line fitting and second, the integrated fluxes are found after Gaussian fitting for He II $\lambda 4686$ and N III $\lambda 4640$. At the top panel of Figure 2, we plot the ratio of the total He II $\lambda 4686$ and N III $\lambda 4640$ integrated flux to the respective integrated flux of the broad H β as a function of rest-frame time with respect to MJD = 59381. The flux is host, continuum, and iron subtracted in both cases (i.e., with and without fitting).

The top panel of Figure 2 shows that there is enhanced emission in the region around 4680 Å (relative to H β) consistent with BF brightening. This enhanced emission lasts for at least 27 rest-frame days after the Keck spectrum and 58 rest-frame days after the initial transient detection. The ratio of the flux of the BF features to H β appears to become weaker than the respective ratio in the LAMOST spectrum after 35 rest-frame days from the Keck spectrum, but it is evident that the emission around 4680 Å still exists. The lower resolution of the FLOYDS spectra compared to LAMOST and Keck may under-predict our measured ratios due to blending with Fe features.

We now turn to investigate the high ionization iron lines. These lines have been seen in the past in AGN and for Fe X $\lambda 6375$ it has been found that the maximum $F([\text{Fe X}] \lambda 6375)/F([\text{O III}] \lambda 5007)$ ratio is ~ 0.24 (Nagao et al. 2000). The LAMOST spectrum of AT2021loi shows a $F([\text{Fe X}] \lambda 6375)/F([\text{O III}] \lambda 5007)$ ratio of ~ 0.6 . In the Keck spectrum, we find this value to be 2.06.

In the LAMOST spectrum, the FWHM of Fe X $\lambda 6375$ is $\sim 1900 \text{ km s}^{-1}$ is lower than that of H β , H α , He I ($\sim 3000 \text{ km s}^{-1}$) and of that of the BF lines (He II $\lambda 4686 + \text{N III } \lambda 4640 \sim 7000 \text{ km s}^{-1}$). For the Keck spectrum, the Fe X $\lambda 6375$ emission line's FWHM is $\sim 2000 \text{ km s}^{-1}$. We note that this is surprising for two reasons: 1) The line seems almost unchanged between

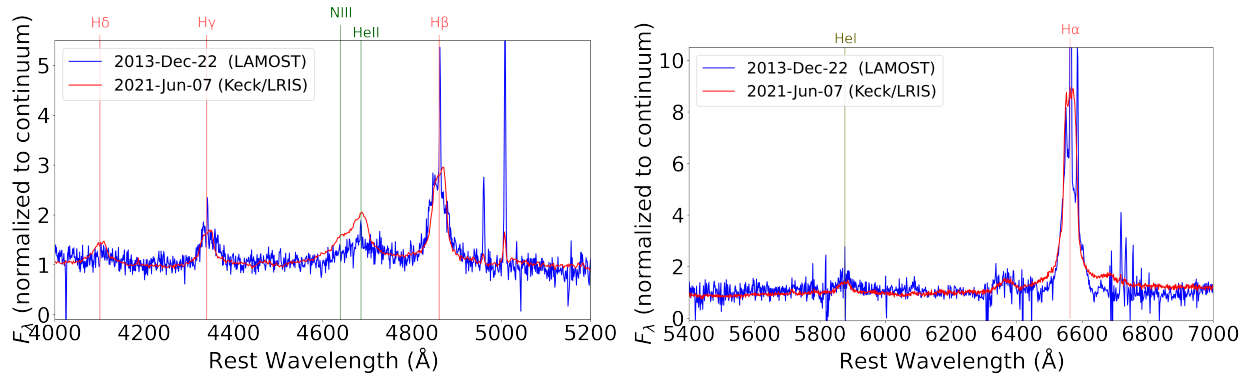


Figure 10. Comparison of the host-subtracted and extinction corrected LAMOST and Keck spectra divided by the power-law continuum and the iron complex as fitted by PYQSOFIT. We see that there is indeed enhanced emission in the region around 4680 Å but also for H δ , with regards to H β . The H α remains essentially unchanged.

Table 3. Emission line ratios from the LAMOST and Keck spectra.

Flux Ratio	Pre-flare	Transient state
$F(\text{H}\alpha^b)/F(\text{H}\beta^b)$	2.33 ± 0.21	2.12 ± 0.34
$F(\text{He II } \lambda 4686)/F(\text{H}\beta^b)$	-	0.71 ± 0.09
$F(\text{N III } \lambda 4640)/F(\text{H}\beta^b)$	-	0.47 ± 0.07
$F(\text{He II } \lambda 4686 + \text{N III } \lambda 4640)/F(\text{H}\beta^b)$	0.58 ± 0.13	1.12 ± 0.05
$F(\text{H}\gamma)/F(\text{H}\beta^b)$	0.48 ± 0.03	0.41 ± 0.02
$F(\text{H}\delta)/F(\text{H}\beta^b)$	0.24 ± 0.02	0.36 ± 0.03

NOTE—For the ratios on this table, we use fluxes from Gaussian fitting. The superscript ‘b’ denotes the broad component.

the two spectra, and 2) in both cases, the line is consistent with a BLR, whereas in Wang et al. (2012), coronal emitters are found to have Fe x $\lambda 6375$ with FWHM between 200 and 1000 km s $^{-1}$, i.e., consistent with the narrow line region (NLR).

5. DISCUSSION

AT 2021loi is an optically-discovered, UV-bright flare observed at the center of an active galaxy. The steep rise in the optical by a factor of ~ 4 in about 40 days, as well as in the UV (a factor of ~ 20 brightening), distinguishes AT 2021loi from the usual variability of unobscured, broad-line AGN, which typically vary by only a few percent over such timescales (MacLeod et al. 2012a; van Velzen et al. 2019). The double-peaked emission feature around 4680 Å seen in the post-peak Keck/LRIS spectrum classifies this nuclear event as a BFF in a galaxy hosting an AGN. In this section, we discuss our key findings regarding AT 2021loi in the context of other types of BF nuclear transients.

5.1. AT 2021loi as a BFF

Here we refer to the basic properties of AT 2021loi that suggest it is part of the BFF class, and compare it to previously reported BFFs. We focus on the three events used by Trakhtenbrot et al. (2019b) to identify this class, namely: AT 2017bgt (first reported in Trakhtenbrot et al. 2019b), F01007-2237 (Tadhunter et al. 2017) and OGLE17aaj (Gromadzki et al. 2019).

After the initial increase in brightness, AT 2021loi shows a very slow decline until the rebrightening ~ 13 months after the initial detection (see Figures 1, 2 and Section 4.1). The slow decline is comparable to that of the BFFs presented in Trakhtenbrot et al. (2019b) i.e., after more than a year, the optical transient emission still persists. In Figure 11, we present the r -band lightcurve of AT 2021loi along with those of the Trakhtenbrot et al. (2019b) BFFs. The rebrightening and second peak are very clear for AT 2021loi. There is evidence for a rebrightening in F01004-2237, too, which we point out explicitly here for the first time. However, in this case the photometric cadence is rather low and the host subtraction is more challenging. The most up-to-date ZTF and ATLAS photometry for AT 2017bgt is also indicative of another bump, roughly 14 months after the initial detection (and thirteen months after the first peak), however this possible rebrightening is even less robust than the one in F01004-2237.²⁰ A late-time rebrightening of the (optical) emission may thus emerge as another intriguing common property of BFFs, although the evidence in hand is still limited.

The optical spectroscopy of AT 2021loi shows a prominent double-peak emission feature around 4680 Å, consistent with blended He II $\lambda 4686$ and N III $\lambda 4640$ emission. The spectra also show other BF features such as O III lines at 3133 and 3444 Å. A strong feature

²⁰ The data showing this secondary peak of AT 2017bgt was not available during the analysis of Trakhtenbrot et al. (2019b).

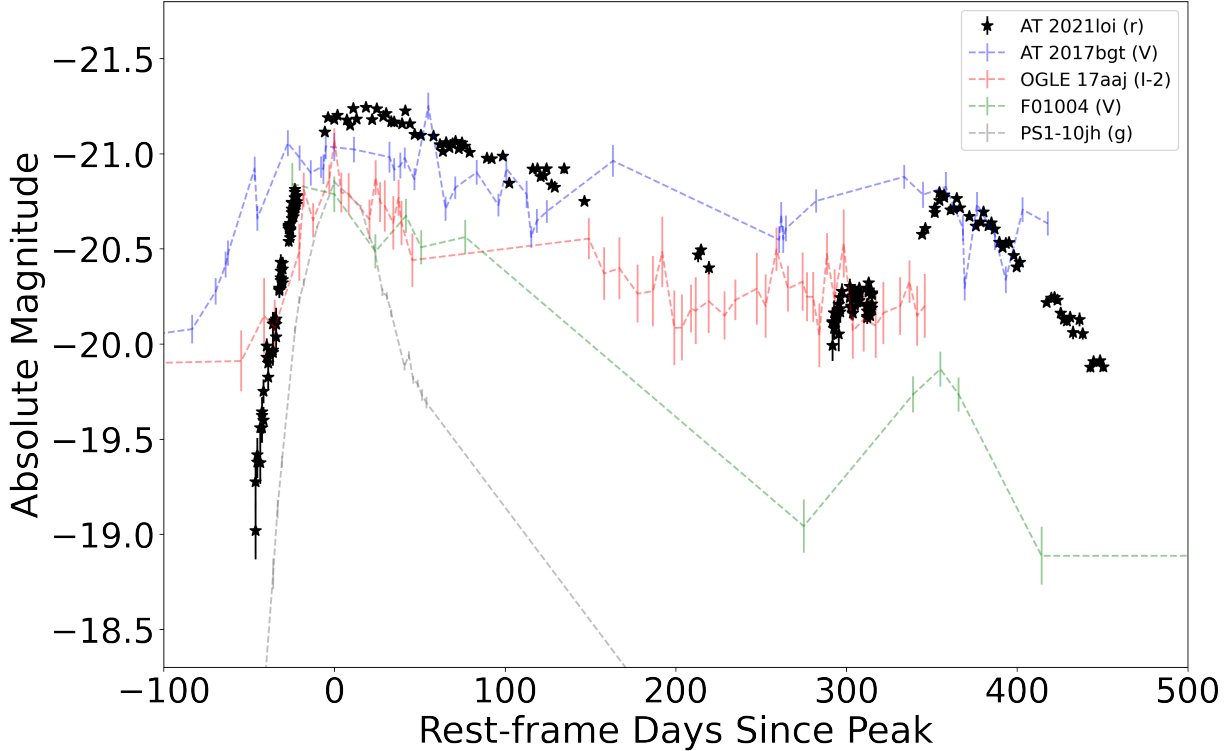


Figure 11. Comparison of the lightcurve of AT 2021loi with those of the BFFs listed in (Tadhunter et al. 2017; Trakhtenbrot et al. 2019b; Gromadzki et al. 2019) and the TDE PS1-10jh (Gezari et al. 2012, 2015). All the magnitudes are reference subtracted. From the lightcurves, we find that although AT 2021loi has a fast rise, it shows a very slow decline similar to other BFFs and unlike a typical TDE.

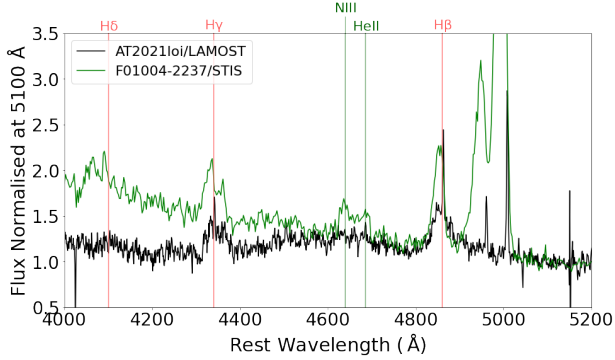


Figure 12. Comparison of the pre-flare LAMOST spectrum of AT 2021loi with the pre-flare *HST* spectrum of F01004-2237 (Tadhunter et al. 2017). Both show pre-flare emission features around 4680 Å.

around 4680 Å is also seen in the pre-flare spectrum of AT 2021loi. To our knowledge, only one of the three BFFs studied by Trakhtenbrot et al. (2019b) has pre-flare optical spectroscopy – the *HST*/STIS spectrum of F01004-2237 (Tadhunter et al. 2017). That spectrum also shows pre-existing N III λ 4640 and He II λ 4686 features, that became stronger following the optical flare. Tadhunter et al. (2017) attributed the pre-existing N III λ 4640 and He II λ 4686 BF emission to WN Wolf-

Rayet stars in the host galaxy, interpreting the flare and He II λ 4686 enhancement as a result of a TDE in F01004-2237.

The pre-flare $F(\text{He II } \lambda 4686 + \text{N III } \lambda 4640)/F(\text{H}\beta)$ ratio of AT 2021loi (0.58) is already higher than what is expected for AGN (~ 0.05 ; see, e.g., Vanden Berk et al. 2001) and is similar to that measured for F01004-2237 (0.49, pre-flare). For AT 2021loi, this ratio increases to ~ 1.1 near the optical peak, which is slightly lower than what was found in the spectrum of F01004-2237 during its flare (~ 1.8) and slightly higher than what was found for OGLE17aaj (~ 0.9 ; Gromadzki et al. 2019).

In Figure 13 we compare the near-peak spectrum of AT 2021loi with those of the BFFs discussed in Trakhtenbrot et al. (2019b). In addition to the ~ 4680 Å feature, AT 2021loi also shows a broad and possibly double-peaked feature near H δ , similar to what is seen for OGLE17aaj (Gromadzki et al. 2019). As previously mentioned, the H δ emission line coincides with the N III BF features expected at 4097 and 4104 Å. These two lines are expected to have relative intensities to N III λ 4640 of 0.117 and 0.082 (respectively; Netzer et al. 1985). Given the limited resolution of the AT 2021loi spectra in hand, it is not possible to properly decompose these lines from H δ but we suggest that since the

$F(\text{H}\delta)/F(\text{H}\beta)$ ratio increased more from pre- to during-flare spectra than the $F(\text{H}\gamma)/F(\text{H}\beta)$ ratio, the $\text{H}\delta$ spectral feature is affected by intensified N III emission.

AT 2021loi also shows signs of enhanced emission (between pre-flare and during-flare spectra) in some higher ionization, coronal lines, specifically $\text{Fe X } \lambda 6375$. This line was also found in the BF nuclear transient AT 2019avd (Malyali et al. 2021). In that case, the presence of coronal emission lines was argued to require, and be associated with, the intense soft X-ray radiation seen in that event. The initial discovery of the X-ray flare by e-Rosita measured an $0.2 - 2$ keV luminosity of $2.7 \times 10^{42} \text{ erg s}^{-1}$, which is 90 times brighter than their pre-flare upper limits. The X-ray emission of AT 2019avd remained rather steady for four months, after which it further increased ($L(0.2 - 2 \text{ keV}) = 1.9 \times 10^{43} \text{ erg s}^{-1}$). For AT 2021loi, there is no X-ray emission detected by our *Swift*/XRT monitoring, with 3σ upper limits in the range $(1.5 - 5.8) \times 10^{42} \text{ erg s}^{-1}$ at $2 - 10$ keV. While there is no X-ray emission detected, we note that the *expected* X-ray luminosity for AT 2021loi at 2 keV, based on the NUV flux ($\nu L_\nu \approx 2.2 \times 10^{43} \text{ erg s}^{-1}$, see Section 4.1), is higher than what was detected in AT 2017bgt ($L(2 - 10 \text{ keV}) = 1.2 \times 10^{43} \text{ erg s}^{-1}$) and in AT 2019avd ($2.7 \times 10^{42} \text{ erg s}^{-1}$).

Thus, the X-ray emission from AT 2021loi and from the AGN in its pre-flare state is either intrinsically weaker than what is seen in normal, persistently accreting AGN (taking into account the ≈ 0.6 dex uncertainty on the expected X-ray emission; see above); is considerably weaker than what is seen in other BFFs; and/or is delayed compared with what is seen in other BFFs. It is highly unlikely that intrinsically luminous X-ray radiation is obscured by (dusty) gas along our line-of-sight, given the prominent blue continuum and broad line emission. Finally, we cannot rule out a more complex scenario in which the X-ray emitting corona was disrupted by the UV flare, as suggested in at least one other AGN-related UV-luminous transient (Ricci et al. 2020). At any rate, the X-ray non-detection following the UV-luminous flare in AT 2021loi does not follow what is seen in normal AGNs.

AT 2021loi is associated with increased UV emission (by a factor of ~ 20) compared to the archival GALEX measurement of its host. The pre-flare optical spectrum clearly shows the presence of an actively accreting SMBH in the nucleus of the host galaxy. The rise of the UV emission, peaking at $\nu L_\nu \approx 2.3 \times 10^{44} \text{ erg s}^{-1}$, combined with the simultaneous and significant brightening of the Bowen features, strongly suggests that the AT 2021loi BF features are driven by the accretion flow onto the SMBH.

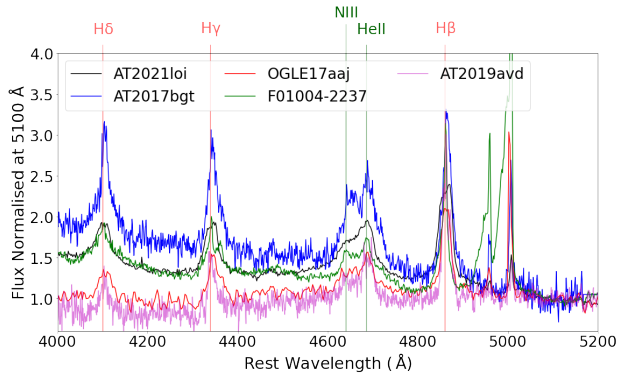


Figure 13. Comparison of the AT 2021loi spectrum (in blue), taken a month after discovery, with the optical spectra of the three BFFs discussed in Trakhtenbrot et al. (2019b).

We can use the observed and modeled SEDs of AT 2021loi to assess whether there is indeed sufficient EUV emission to account for the BF features. First, by integrating the best-fit ($17.2 \times 10^3 \text{ K}$) blackbody SED of the flare near peak, we find that only $\sim 10^{-12}$ of the total luminosity is emitted below 228 \AA (the range required to ionize He II), corresponding to a luminosity of the order of $10^{32} \text{ erg s}^{-1}$. The observed Bowen lines near peak, however, have respective ($\text{He II } \lambda 4686$ and $\text{N III } \lambda 4640$) luminosities of order $10^{41} \text{ erg s}^{-1}$. Thus, another ionizing source, outside the measured blackbody continuum, might be required to account for the BF emission. This is similar to what was found for the BF-emitting TDE AT 2018dyb (Leloudas et al. 2019).

Second, we can use a (simplified) AGN SED to assess the radiative (EUV) energetics, scaling to either the pre- or during-flare measured luminosities of AT 2021loi. We use the Marconi et al. (2004) SED, scaled to either $\log(L_{\text{bol}}/\text{erg s}^{-1}) = 43.48$ or 44.46 for the pre-flare or the during-flare states (respectively). The integrated EUV luminosities, i.e. over $\lambda < 228 \text{ \AA}$, are 7.4×10^{42} and $5.3 \times 10^{43} \text{ erg s}^{-1}$, for the pre- and during-flare, near peak states (respectively). At face value, it appears that the EUV emission from the AGN is sufficient to account for the energetics of the BF features ($\gtrsim 10^{41} \text{ erg s}^{-1}$), even before the optical/UV flare. However, given that the (optical) luminosity of the pre-existing AGN in this system is not exceptionally high, we recall that BF lines are *not* ubiquitous in persistent AGN (e.g., Netzer et al. 1985; Vanden Berk et al. 2001), suggesting that other considerations apart from pure (radiative, EUV) energetics are at play.

5.2. Comparison to TDEs

We next compare AT 2021loi to the growing sample of TDEs detected in the optical/UV regime (see van Velzen et al. 2020 and Gezari 2021 for recent reviews).

The rise time of AT 2021loi, of about a month, is similar to what is observed in optical/UV TDEs. However, the decline of the optical emission in AT 2021loi, which can be described by a power law with index shallower than $\alpha \simeq -0.8$ (second decline $\alpha \simeq -0.9$), is much slower than what is seen in optical/UV TDEs, which are typically compared to $\alpha \simeq -5/3$. This is also apparent in Figure 11, where we compare the optical/UV lightcurve of AT 2021loi with that of the TDE PS1-10jh (Gezari et al. 2012, 2015). The TDE lightcurve fades within a few months, whereas AT 2021loi lasts for more than one year, and also presents a secondary brightening. If we fit the post-peak decline of AT 2021loi with a $t^{-5/3}$ power-law, the required disruption time is at $\text{MJD} = 59031 \pm 11$ (i.e., 2020 June–July), which is approximately one year before the initial ZTF detection of the flare. While the tidal disruptions of *giant* stars are indeed expected to have longer time scales (e.g.; MacLeod et al. 2012b), this would also imply longer rise times (i.e. months instead of weeks), which is not the case with AT 2021loi. We conclude that the optical/UV lightcurve of AT 2021loi is markedly different than what is seen in (optical/UV) TDEs. We conclude that the overall shape of the AT 2021loi is very different from what we know so far for TDEs.

In terms of spectral properties, in many cases optical/UV TDEs also show broad emission features around 4680\AA (associated with He II $\lambda 4686$ and N III $\lambda 4640$; see van Velzen et al. 2020 and references therein). However, we first note that the emission lines (such as He II and Balmer) in TDEs ($\text{FWHM} \sim 10^4 \text{ km s}^{-1}$) are much broader than those observed in AT 2021loi ($\text{FWHM} \sim 3000 \text{ km s}^{-1}$). In terms of broad-band SEDs, the color of AT 2021loi is redder than what is found for TDEs in the early stages and shows very limited evolution (Figure 6). When modeling the transient emission in AT 2021loi with a blackbody, we find that the derived temperature is much lower than what is seen in TDEs, whereas its (peak) bolometric luminosity and its inferred blackbody radius are higher than in TDEs (see Section 4.1). These features lend further support to our interpretation that the transient emission in AT 2021loi is not driven by a TDE – at least not of the common optical/UV kind – as emphasized by Trakhtenbrot et al. (2019a) for the BFF class as a whole.

AT 2021loi is also not compatible with scenarios of partial tidal disruption events (e.g. Zhong et al. 2022), double tidal disruption events (e.g. Mandel & Levin 2015) or extreme mass-ratio inspirals (EMRIs; e.g., Sari & Fragione 2019). The second peak in AT 2021loi occurred ~ 400 days after the first peak, which is longer than predicted in the partial TDEs scenarios (i.e., $\lesssim 150$

days for main sequence stars). On the other hand, in the case of EMRIs, repeated flares are expected to happen on longer timescales (i.e., \gtrsim several years). However, more detailed simulations of such events are needed to investigate their possible emission signatures.

6. CONCLUSIONS

We presented multi-epoch observations of the nuclear transient AT 2021loi, whose main observed photometric and spectroscopic characteristics are as follows:

1. AT 2021loi is a transient event in a previously known broad-line AGN (WISEA J010039.62+394230.3). An archival spectrum shows clear broad H α , H β and H γ emission and a bump around 4680\AA which suggests that at least He II $\lambda 4686$ was present before the flare.
2. AT 2021loi shows a rapid (\sim month) rise of the optical flux by a factor of $\sim 4\times$ and a rise in the UV by a factor of $\sim 20\times$ while no previous strong variability is found (Figure 1). AT 2021loi shows a very slow decline for thirteen months after the initial detection (about twelve months after the peak). Then the optical/UV lightcurve shows a rebrightening and a second peak about 390 days after the first one.
3. The spectra during the transient phase show enhanced broad H α , H β , H γ and H δ emission. We also find enhanced He I emission at 5875\AA .
4. The spectra of the source during the flare also show BF lines such as N III $\lambda 4640$ and O III $\lambda 3133$.
5. The flare spectroscopy also reveals signs for enhanced emission from higher ionization coronal lines such as Fe X $\lambda 6375$. The width of this line is consistent with that of other broad lines (i.e., originating from the BLR), unlike what has been seen in AGN until now.
6. AT 2021loi shows no X-ray emission down to a limit of $L(2 - 10 \text{ keV}) < 2.5 \times 10^{42} \text{ erg s}^{-1}$ (3σ) which is considerably lower (by a factor of ~ 25) than what is expected from the UV-to-X-ray scaling relations of normal AGN.

AT 2021loi adds further insight, but also raises new questions, related to the already complex phenomenology of SMBH-related transients and extreme AGN variability. Continued monitoring of AT 2021loi could provide insights as to its multi-peak nature, testing models of repeated flaring activity. Any late-time X-ray or radio emission could provide further clues as to the nature of this event, and perhaps the class of BFFs as a whole.

L.M., B.T., I.A. and M.C.L. acknowledge support from the European Research Council (ERC) under the European Union’s Horizon 2020 research and innovation program (grant agreements 852097 and 950533) and from the Israel Science Foundation (grant numbers 1849/19 and 2752/19). I.A. is a CIFAR Azrieli Global Scholar in the Gravity and the Extreme Universe Program and acknowledges support from that program, from the United States—Israel Binational Science Foundation (BSF), and from the Israeli Council for Higher Education Alon Fellowship. C.R. acknowledges support from the Fondecyt Iniciacion grant 11190831 and ANID BASAL project FB210003. A.H. is grateful for the support by the I-Core Program of the Planning and Budgeting Committee and the Israel Science Foundation, and support by ISF grant 647/18. A.H. is grateful for support by the Zelman Cowen Academic Initiatives. This publication was made possible through the support of an LSSTC Catalyst Fellowship to K.A.B funded through Grant 62192 from the John Templeton Foundation to LSST Corporation. The opinions expressed in this publication are those of the author(s) and do not necessarily reflect the views of LSSTC or the John Templeton Foundation.

Guoshoujing Telescope (the Large Sky Area Multi-Object Fiber Spectroscopic Telescope LAMOST) is a National Major Scientific Project built by the Chinese Academy of Sciences. Funding for the project has been provided by the National Development and Reform Commission. LAMOST is operated and managed by the National Astronomical Observatories, Chinese Academy of Sciences. The ZTF forced-photometry service was funded under the Heising-Simons Foundation grant No. 12540303 (PI: Graham). This work makes use of data from the Las Cumbres Observatory global telescope network. The LCO group is supported by NSF grant AST-1911151 and AST-1911225 and NASA Swift grant 80NSSC19k1639. The National Radio Astronomy Observatory is a facility of the National Science Foundation operated under cooperative agreement by

Associated Universities, Inc. We acknowledge the staff who operate and run the AMI-LA telescope at Lord’s Bridge, Cambridge, for the AMI-LA radio data. AMI is supported by the Universities of Cambridge and Oxford, and by the European Research Council under grant ERC-2012-StG307215 LODESTONE.

This work made use of data from the Asteroid Terrestrial- impact Last Alert System (ATLAS) project. ATLAS is primarily funded to search for near earth asteroids through NASA grants NN12AR55G, 80NSSC18K0284, and 80NSSC18K1575; by-products of the NEO search include images and catalogs from the survey area. This work was partially funded by Kepler/K2 grant J1944/80NSSC19K0112 and HST GO-15889, and STFC grants ST/T000198/1 and ST/S006109/1. The ATLAS science products have been made possible through the contributions of the University of Hawaii Institute for Astronomy, the Queen’s University Belfast, the Space Telescope Science Institute, the South African Astronomical Observatory, and The Millennium Institute of Astrophysics (MAS), Chile.

This work also made use of the NASA/IPAC Extragalactic Database (NED), which is funded by the National Aeronautics and Space Administration and operated by the California Institute of Technology, and of data, software and web tools obtained from the High Energy Astrophysics Science Archive Research Center (HEASARC), a service of the Astrophysics Science Division at NASA/GSFC and of the Smithsonian Astrophysical Observatory’s High Energy Astrophysics Division.

Software: `AstroPy` (Astropy Collaboration et al. 2013, 2018, 2022), `Matplotlib` (Hunter 2007), `NumPy` (Harris et al. 2020), `SciPy` (Virtanen et al. 2020), `lcogtspipe` (Valenti et al. 2016), `PyQSOFit` (Guo et al. 2018), `ASPIRED` (Lam & Smith 2022)

Facilities: Las Cumbres (FLOYDS, Sinistro), Keck (LRIS), LAMOST, WISE, Swift (UVOT and XRT), ZTF, ATLAS, VLA, AMI-LA

REFERENCES

- Arcavi, I. 2022, *ApJ*, 937, 75,
doi: [10.3847/1538-4357/ac90c0](https://doi.org/10.3847/1538-4357/ac90c0)
- Arcavi, I., Gal-Yam, A., Sullivan, M., et al. 2014, *ApJ*, 793, 38, doi: [10.1088/0004-637X/793/1/38](https://doi.org/10.1088/0004-637X/793/1/38)
- Assef, R. J., Stern, D., Noirot, G., et al. 2018, *ApJS*, 234, 23, doi: [10.3847/1538-4365/aaa00a](https://doi.org/10.3847/1538-4365/aaa00a)
- Astropy Collaboration, Robitaille, T. P., Tollerud, E. J., et al. 2013, *A&A*, 558, A33,
doi: [10.1051/0004-6361/201322068](https://doi.org/10.1051/0004-6361/201322068)
- Astropy Collaboration, Price-Whelan, A. M., Sipőcz, B. M., et al. 2018, *AJ*, 156, 123, doi: [10.3847/1538-3881/aabc4f](https://doi.org/10.3847/1538-3881/aabc4f)
- Astropy Collaboration, Price-Whelan, A. M., Lim, P. L., et al. 2022, *ApJ*, 935, 167, doi: [10.3847/1538-4357/ac7c74](https://doi.org/10.3847/1538-4357/ac7c74)
- Baldwin, J. A., Phillips, M. M., & Terlevich, R. 1981, *PASP*, 93, 5, doi: [10.1086/130766](https://doi.org/10.1086/130766)

- Becker, A. 2015, HOTPANTS: High Order Transform of PSF ANd Template Subtraction, Astrophysics Source Code Library, record ascl:1504.004, <http://ascl.net/1504.004>
- Becker, R. H., White, R. L., & Helfand, D. J. 1994, in *Astronomical Society of the Pacific Conference Series*, Vol. 61, *Astronomical Data Analysis Software and Systems III*, ed. D. R. Crabtree, R. J. Hanisch, & J. Barnes, 165
- Bentz, M. C., Denney, K. D., Grier, C. J., et al. 2013, *ApJ*, 767, 149, doi: [10.1088/0004-637X/767/2/149](https://doi.org/10.1088/0004-637X/767/2/149)
- Blagorodnova, N., Gezari, S., Hung, T., et al. 2017, *ApJ*, 844, 46, doi: [10.3847/1538-4357/aa7579](https://doi.org/10.3847/1538-4357/aa7579)
- Boller, T., Freyberg, M. J., Trümper, J., et al. 2016, *A&A*, 588, A103, doi: [10.1051/0004-6361/201525648](https://doi.org/10.1051/0004-6361/201525648)
- Bowen, I. S. 1928, *ApJ*, 67, 1, doi: [10.1086/143091](https://doi.org/10.1086/143091)
- Brown, T. M., Baliber, N., Bianco, F. B., et al. 2013, *PASP*, 125, 1031, doi: [10.1086/673168](https://doi.org/10.1086/673168)
- Burrows, D. N., Hill, J. E., Nousek, J. A., et al. 2005, *SSRv*, 120, 165, doi: [10.1007/s11214-005-5097-2](https://doi.org/10.1007/s11214-005-5097-2)
- Cannizzaro, G., Fraser, M., Jonker, P. G., et al. 2020, *MNRAS*, 493, 477, doi: [10.1093/mnras/staa186](https://doi.org/10.1093/mnras/staa186)
- Caplar, N., Lilly, S. J., & Trakhtenbrot, B. 2017, *ApJ*, 834, 111, doi: [10.3847/1538-4357/834/2/111](https://doi.org/10.3847/1538-4357/834/2/111)
- Cardelli, J. A., Clayton, G. C., & Mathis, J. S. 1989, *ApJ*, 345, 245, doi: [10.1086/167900](https://doi.org/10.1086/167900)
- Clavel, J., Reichert, G. A., Alloin, D., et al. 1991, *ApJ*, 366, 64, doi: [10.1086/169540](https://doi.org/10.1086/169540)
- Condon, J. J., Cotton, W. D., Greisen, E. W., et al. 1998, *AJ*, 115, 1693, doi: [10.1086/300337](https://doi.org/10.1086/300337)
- Cutri, R. M., Wright, E. L., Conrow, T., et al. 2021, *VizieR Online Data Catalog*, II/328
- Dexter, J., & Agol, E. 2011, *ApJL*, 727, L24, doi: [10.1088/2041-8205/727/1/L24](https://doi.org/10.1088/2041-8205/727/1/L24)
- Duras, F., Bongiorno, A., Ricci, F., et al. 2020, *A&A*, 636, A73, doi: [10.1051/0004-6361/201936817](https://doi.org/10.1051/0004-6361/201936817)
- Fahlman, G. G., & Ulrych, T. J. 1975, *ApJ*, 201, 277, doi: [10.1086/153884](https://doi.org/10.1086/153884)
- Förster, F., Cabrera-Vives, G., Castillo-Navarrete, E., et al. 2021, *AJ*, 161, 242, doi: [10.3847/1538-3881/abe9bc](https://doi.org/10.3847/1538-3881/abe9bc)
- Frederick, S., Gezari, S., Graham, M. J., et al. 2021, *ApJ*, 920, 56, doi: [10.3847/1538-4357/ac110f](https://doi.org/10.3847/1538-4357/ac110f)
- Gehrels, N., Chincarini, G., Giommi, P., et al. 2004, *ApJ*, 611, 1005, doi: [10.1086/422091](https://doi.org/10.1086/422091)
- Gezari, S. 2021, *ARA&A*, 59, 21, doi: [10.1146/annurev-astro-111720-030029](https://doi.org/10.1146/annurev-astro-111720-030029)
- Gezari, S., Chornock, R., Lawrence, A., et al. 2015, *ApJL*, 815, L5, doi: [10.1088/2041-8205/815/1/L5](https://doi.org/10.1088/2041-8205/815/1/L5)
- Gezari, S., Chornock, R., Rest, A., et al. 2012, *Nature*, 485, 217, doi: [10.1038/nature10990](https://doi.org/10.1038/nature10990)
- Graham, M., Yao, Y., Velzen, S. V., et al. 2021, *Transient Name Server Classification Report*, 2021-2018, 1
- Graham, M. J., Djorgovski, S. G., Drake, A. J., et al. 2017, *MNRAS*, 470, 4112, doi: [10.1093/mnras/stx1456](https://doi.org/10.1093/mnras/stx1456)
- Graham, M. J., Ross, N. P., Stern, D., et al. 2020, *MNRAS*, 491, 4925, doi: [10.1093/mnras/stz3244](https://doi.org/10.1093/mnras/stz3244)
- Greene, J. E., & Ho, L. C. 2005, *ApJ*, 630, 122, doi: [10.1086/431897](https://doi.org/10.1086/431897)
- Gromadzki, M., Hamanowicz, A., Wyrzykowski, L., et al. 2019, *A&A*, 622, L2, doi: [10.1051/0004-6361/201833682](https://doi.org/10.1051/0004-6361/201833682)
- Guo, H., Shen, Y., & Wang, S. 2018, *PyQSOFit: Python code to fit the spectrum of quasars*, <http://ascl.net/1809.008>
- Harris, C. R., Millman, K. J., van der Walt, S. J., et al. 2020, *Nature*, 585, 357, doi: [10.1038/s41586-020-2649-2](https://doi.org/10.1038/s41586-020-2649-2)
- Hawkins, M. R. S. 1993, *Nature*, 366, 242, doi: [10.1038/366242a0](https://doi.org/10.1038/366242a0)
- Hickish, J., Razavi-Ghods, N., Perrott, Y. C., et al. 2018, *MNRAS*, 475, 5677, doi: [10.1093/mnras/sty074](https://doi.org/10.1093/mnras/sty074)
- Horne, K. 1986, *PASP*, 98, 609, doi: [10.1086/131801](https://doi.org/10.1086/131801)
- Hunter, J. D. 2007, *Computing In Science & Engineering*, 9, 90, doi: [10.1109/MCSE.2007.55](https://doi.org/10.1109/MCSE.2007.55)
- Just, D. W., Brandt, W. N., Shemmer, O., et al. 2007, *ApJ*, 665, 1004, doi: [10.1086/519990](https://doi.org/10.1086/519990)
- Kaspi, S., Smith, P. S., Netzer, H., et al. 2000, *ApJ*, 533, 631, doi: [10.1086/308704](https://doi.org/10.1086/308704)
- Kawaguchi, T., Mineshige, S., Umemura, M., & Turner, E. L. 1998, *ApJ*, 504, 671, doi: [10.1086/306105](https://doi.org/10.1086/306105)
- Kewley, L. J., Groves, B., Kauffmann, G., & Heckman, T. 2006, *MNRAS*, 372, 961, doi: [10.1111/j.1365-2966.2006.10859.x](https://doi.org/10.1111/j.1365-2966.2006.10859.x)
- Koshida, S., Minezaki, T., Yoshii, Y., et al. 2014, *ApJ*, 788, 159, doi: [10.1088/0004-637X/788/2/159](https://doi.org/10.1088/0004-637X/788/2/159)
- Krolik, J. H., Horne, K., Kallman, T. R., et al. 1991, *ApJ*, 371, 541, doi: [10.1086/169918](https://doi.org/10.1086/169918)
- Lam, M. C., & Smith, R. J. 2022, *ASPIRED: A Python-based spectral data reduction toolkit, 0.4.6*, Zenodo, doi: [10.5281/zenodo.6903357](https://doi.org/10.5281/zenodo.6903357)
- Lam, M. C., Smith, R. J., Arcavi, I., et al. 2021, *arXiv e-prints*, arXiv:2111.02127, <https://arxiv.org/abs/2111.02127>
- LaMassa, S. M., Cales, S., Moran, E. C., et al. 2015, *ApJ*, 800, 144, doi: [10.1088/0004-637X/800/2/144](https://doi.org/10.1088/0004-637X/800/2/144)
- Lawrence, A. 2018, *Nature Astronomy*, 2, 102, doi: [10.1038/s41550-017-0372-1](https://doi.org/10.1038/s41550-017-0372-1)
- Leloudas, G., Dai, L., Arcavi, I., et al. 2019, *ApJ*, 887, 218, doi: [10.3847/1538-4357/ab5792](https://doi.org/10.3847/1538-4357/ab5792)
- Luo, B., Brandt, W. N., Hall, P. B., et al. 2015, *ApJ*, 805, 122, doi: [10.1088/0004-637X/805/2/122](https://doi.org/10.1088/0004-637X/805/2/122)

- Lusso, E., & Risaliti, G. 2016, *ApJ*, 819, 154, doi: [10.3847/0004-637X/819/2/154](https://doi.org/10.3847/0004-637X/819/2/154)
- MacLeod, C. L., Ivezić, Ž., Kochanek, C. S., et al. 2010, *ApJ*, 721, 1014, doi: [10.1088/0004-637X/721/2/1014](https://doi.org/10.1088/0004-637X/721/2/1014)
- MacLeod, C. L., Ivezić, Ž., Sesar, B., et al. 2012a, *ApJ*, 753, 106, doi: [10.1088/0004-637X/753/2/106](https://doi.org/10.1088/0004-637X/753/2/106)
- MacLeod, C. L., Green, P. J., Anderson, S. F., et al. 2019, *ApJ*, 874, 8, doi: [10.3847/1538-4357/ab05e2](https://doi.org/10.3847/1538-4357/ab05e2)
- MacLeod, M., Guillochon, J., & Ramirez-Ruiz, E. 2012b, *ApJ*, 757, 134, doi: [10.1088/0004-637X/757/2/134](https://doi.org/10.1088/0004-637X/757/2/134)
- Mainzer, A., Bauer, J., Grav, T., et al. 2011, *ApJ*, 731, 53, doi: [10.1088/0004-637X/731/1/53](https://doi.org/10.1088/0004-637X/731/1/53)
- Mainzer, A., Bauer, J., Cutri, R. M., et al. 2014, *ApJ*, 792, 30, doi: [10.1088/0004-637X/792/1/30](https://doi.org/10.1088/0004-637X/792/1/30)
- Malyali, A., Rau, A., Merloni, A., et al. 2021, *A&A*, 647, A9, doi: [10.1051/0004-6361/202039681](https://doi.org/10.1051/0004-6361/202039681)
- Mandel, I., & Levin, Y. 2015, *ApJL*, 805, L4, doi: [10.1088/2041-8205/805/1/L4](https://doi.org/10.1088/2041-8205/805/1/L4)
- Marconi, A., Risaliti, G., Gilli, R., et al. 2004, *MNRAS*, 351, 169, doi: [10.1111/j.1365-2966.2004.07765.x](https://doi.org/10.1111/j.1365-2966.2004.07765.x)
- McMullin, J. P., Waters, B., Schiebel, D., Young, W., & Golap, K. 2007, in *Astronomical Society of the Pacific Conference Series*, Vol. 376, *Astronomical Data Analysis Software and Systems XVI*, ed. R. A. Shaw, F. Hill, & D. J. Bell, 127
- Mejía-Restrepo, J. E., Trakhtenbrot, B., Lira, P., & Netzer, H. 2018, *MNRAS*, 478, 1929, doi: [10.1093/mnras/sty1086](https://doi.org/10.1093/mnras/sty1086)
- Mejía-Restrepo, J. E., Trakhtenbrot, B., Koss, M. J., et al. 2022, *ApJS*, 261, 5, doi: [10.3847/1538-4365/ac6602](https://doi.org/10.3847/1538-4365/ac6602)
- Mor, R., Netzer, H., & Elitzur, M. 2009, *ApJ*, 705, 298, doi: [10.1088/0004-637X/705/1/298](https://doi.org/10.1088/0004-637X/705/1/298)
- Munoz-Arancibia, A., Forster, F., Bauer, F. E., et al. 2021, *Transient Name Server Discovery Report*, 2021-1503, 1
- Nagao, T., Taniguchi, Y., & Murayama, T. 2000, *AJ*, 119, 2605, doi: [10.1086/301411](https://doi.org/10.1086/301411)
- Nanni, R., Vignali, C., Gilli, R., Moretti, A., & Brandt, W. N. 2017, *A&A*, 603, A128, doi: [10.1051/0004-6361/201730484](https://doi.org/10.1051/0004-6361/201730484)
- Netzer, H., Elitzur, M., & Ferland, G. J. 1985, *ApJ*, 299, 752, doi: [10.1086/163741](https://doi.org/10.1086/163741)
- Netzer, H., Lani, C., Nordon, R., et al. 2016, *ApJ*, 819, 123, doi: [10.3847/0004-637X/819/2/123](https://doi.org/10.3847/0004-637X/819/2/123)
- Nicholl, M. 2018, *Research Notes of the American Astronomical Society*, 2, 230, doi: [10.3847/2515-5172/aaf799](https://doi.org/10.3847/2515-5172/aaf799)
- Oke, J. B. 1974, *ApJS*, 27, 21, doi: [10.1086/190287](https://doi.org/10.1086/190287)
- Oke, J. B., Cohen, J. G., Carr, M., et al. 1995, *PASP*, 107, 375, doi: [10.1086/133562](https://doi.org/10.1086/133562)
- Panessa, F., Baldi, R. D., Laor, A., et al. 2019, *Nature Astronomy*, 3, 387, doi: [10.1038/s41550-019-0765-4](https://doi.org/10.1038/s41550-019-0765-4)
- Pereyra, N. A., Vanden Berk, D. E., Turnshek, D. A., et al. 2006, *ApJ*, 642, 87, doi: [10.1086/500919](https://doi.org/10.1086/500919)
- Perrott, Y. C., Scaife, A. M. M., Green, D. A., et al. 2013, *MNRAS*, 429, 3330, doi: [10.1093/mnras/sts589](https://doi.org/10.1093/mnras/sts589)
- Peterson, B. M., Berlind, P., Bertram, R., et al. 1994, *ApJ*, 425, 622, doi: [10.1086/174009](https://doi.org/10.1086/174009)
- Peterson, B. M., Denney, K. D., De Rosa, G., et al. 2013, *ApJ*, 779, 109, doi: [10.1088/0004-637X/779/2/109](https://doi.org/10.1088/0004-637X/779/2/109)
- Rakshit, S., Stalin, C. S., & Kotilainen, J. 2020, *ApJS*, 249, 17, doi: [10.3847/1538-4365/ab99c5](https://doi.org/10.3847/1538-4365/ab99c5)
- Rees, M. J. 1988, *Nature*, 333, 523, doi: [10.1038/333523a0](https://doi.org/10.1038/333523a0)
- Ricci, C., & Trakhtenbrot, B. 2022, arXiv e-prints, arXiv:2211.05132. <https://arxiv.org/abs/2211.05132>
- Ricci, C., Trakhtenbrot, B., Koss, M. J., et al. 2017, *ApJS*, 233, 17, doi: [10.3847/1538-4365/aa96ad](https://doi.org/10.3847/1538-4365/aa96ad)
- Ricci, C., Kara, E., Loewenstein, M., et al. 2020, *ApJL*, 898, L1, doi: [10.3847/2041-8213/ab91a1](https://doi.org/10.3847/2041-8213/ab91a1)
- Roming, P. W. A., Kennedy, T. E., Mason, K. O., et al. 2005, *SSRv*, 120, 95, doi: [10.1007/s11214-005-5095-4](https://doi.org/10.1007/s11214-005-5095-4)
- Ruan, J. J., Anderson, S. F., Dexter, J., & Agol, E. 2014, *ApJ*, 783, 105, doi: [10.1088/0004-637X/783/2/105](https://doi.org/10.1088/0004-637X/783/2/105)
- Rumbaugh, N., Shen, Y., Morganson, E., et al. 2018, *ApJ*, 854, 160, doi: [10.3847/1538-4357/aaa9b6](https://doi.org/10.3847/1538-4357/aaa9b6)
- Runnoe, J. C., Brotherton, M. S., & Shang, Z. 2012, *MNRAS*, 422, 478, doi: [10.1111/j.1365-2966.2012.20620.x](https://doi.org/10.1111/j.1365-2966.2012.20620.x)
- Sand, D. J., Brown, T., Haynes, R., & Dubberley, M. 2011, in *American Astronomical Society Meeting Abstracts*, Vol. 218, *American Astronomical Society Meeting Abstracts #218*, 132.03
- Sari, R., & Fragione, G. 2019, *ApJ*, 885, 24, doi: [10.3847/1538-4357/ab43df](https://doi.org/10.3847/1538-4357/ab43df)
- Schlafly, E. F., & Finkbeiner, D. P. 2011, *ApJ*, 737, 103, doi: [10.1088/0004-637X/737/2/103](https://doi.org/10.1088/0004-637X/737/2/103)
- Shen, Y. 2013, *Bulletin of the Astronomical Society of India*, 41, 61, doi: [10.48550/arXiv.1302.2643](https://doi.org/10.48550/arXiv.1302.2643)
- Shen, Y., Greene, J. E., Strauss, M. A., Richards, G. T., & Schneider, D. P. 2008, *ApJ*, 680, 169, doi: [10.1086/587475](https://doi.org/10.1086/587475)
- Shen, Y., Richards, G. T., Strauss, M. A., et al. 2011, *ApJS*, 194, 45, doi: [10.1088/0067-0049/194/2/45](https://doi.org/10.1088/0067-0049/194/2/45)
- Smith, K. L., Mushotzky, R. F., Koss, M., et al. 2020, *MNRAS*, 492, 4216, doi: [10.1093/mnras/stz3608](https://doi.org/10.1093/mnras/stz3608)
- Stern, D., Assef, R. J., Benford, D. J., et al. 2012, *ApJ*, 753, 30, doi: [10.1088/0004-637X/753/1/30](https://doi.org/10.1088/0004-637X/753/1/30)
- Suganuma, M., Yoshii, Y., Kobayashi, Y., et al. 2006, *ApJ*, 639, 46, doi: [10.1086/499326](https://doi.org/10.1086/499326)
- Tadhunter, C., Spence, R., Rose, M., Mullaney, J., & Crowther, P. 2017, *Nature Astronomy*, 1, 0061, doi: [10.1038/s41550-017-0061](https://doi.org/10.1038/s41550-017-0061)
- Tonry, J. L., Denneau, L., Heinze, A. N., et al. 2018, *PASP*, 130, 064505, doi: [10.1088/1538-3873/aabadf](https://doi.org/10.1088/1538-3873/aabadf)

- Trakhtenbrot, B., & Netzer, H. 2012a, MNRAS, 427, 3081, doi: [10.1111/j.1365-2966.2012.22056.x](https://doi.org/10.1111/j.1365-2966.2012.22056.x)
- . 2012b, MNRAS, 427, 3081, doi: [10.1111/j.1365-2966.2012.22056.x](https://doi.org/10.1111/j.1365-2966.2012.22056.x)
- Trakhtenbrot, B., Arcavi, I., MacLeod, C. L., et al. 2019a, ApJ, 883, 94, doi: [10.3847/1538-4357/ab39e4](https://doi.org/10.3847/1538-4357/ab39e4)
- Trakhtenbrot, B., Arcavi, I., Ricci, C., et al. 2019b, Nature Astronomy, 3, 242, doi: [10.1038/s41550-018-0661-3](https://doi.org/10.1038/s41550-018-0661-3)
- Valenti, S., Howell, D. A., Stritzinger, M. D., et al. 2016, MNRAS, 459, 3939, doi: [10.1093/mnras/stw870](https://doi.org/10.1093/mnras/stw870)
- van Velzen, S., Holoien, T. W. S., Onori, F., Hung, T., & Arcavi, I. 2020, SSRv, 216, 124, doi: [10.1007/s11214-020-00753-z](https://doi.org/10.1007/s11214-020-00753-z)
- van Velzen, S., Gezari, S., Cenko, S. B., et al. 2019, ApJ, 872, 198, doi: [10.3847/1538-4357/aafe0c](https://doi.org/10.3847/1538-4357/aafe0c)
- Vanden Berk, D. E., Richards, G. T., Bauer, A., et al. 2001, AJ, 122, 549, doi: [10.1086/321167](https://doi.org/10.1086/321167)
- Veitch-Michaelis, J., & Lam, M. C. 2021, Rascal, 0.3.0, Zenodo, doi: [10.5281/zenodo.4124170](https://doi.org/10.5281/zenodo.4124170)
- Veitch-Michaelis, J., & Lam, M. C. 2020, in Astronomical Society of the Pacific Conference Series, Vol. 527, Astronomical Data Analysis Software and Systems XXIX, ed. R. Pizzo, E. R. Deul, J. D. Mol, J. de Plaa, & H. Verkouter, 627. <https://arxiv.org/abs/1912.05883>
- Virtanen, P., Gommers, R., Oliphant, T. E., et al. 2020, Nature Methods, 17, 261, doi: [10.1038/s41592-019-0686-2](https://doi.org/10.1038/s41592-019-0686-2)
- Wang, T.-G., Zhou, H.-Y., Komossa, S., et al. 2012, ApJ, 749, 115, doi: [10.1088/0004-637X/749/2/115](https://doi.org/10.1088/0004-637X/749/2/115)
- Wright, E. L., Eisenhardt, P. R. M., Mainzer, A. K., et al. 2010, AJ, 140, 1868, doi: [10.1088/0004-6256/140/6/1868](https://doi.org/10.1088/0004-6256/140/6/1868)
- York, D. G., Adelman, J., Anderson, John E., J., et al. 2000, AJ, 120, 1579, doi: [10.1086/301513](https://doi.org/10.1086/301513)
- Zhao, G., Zhao, Y.-H., Chu, Y.-Q., Jing, Y.-P., & Deng, L.-C. 2012, Research in Astronomy and Astrophysics, 12, 723, doi: [10.1088/1674-4527/12/7/002](https://doi.org/10.1088/1674-4527/12/7/002)
- Zhong, S., Li, S., Berczik, P., & Spurzem, R. 2022, ApJ, 933, 96, doi: [10.3847/1538-4357/ac71ad](https://doi.org/10.3847/1538-4357/ac71ad)
- Zwart, J. T. L., Barker, R. W., Biddulph, P., et al. 2008, MNRAS, 391, 1545, doi: [10.1111/j.1365-2966.2008.13953.x](https://doi.org/10.1111/j.1365-2966.2008.13953.x)

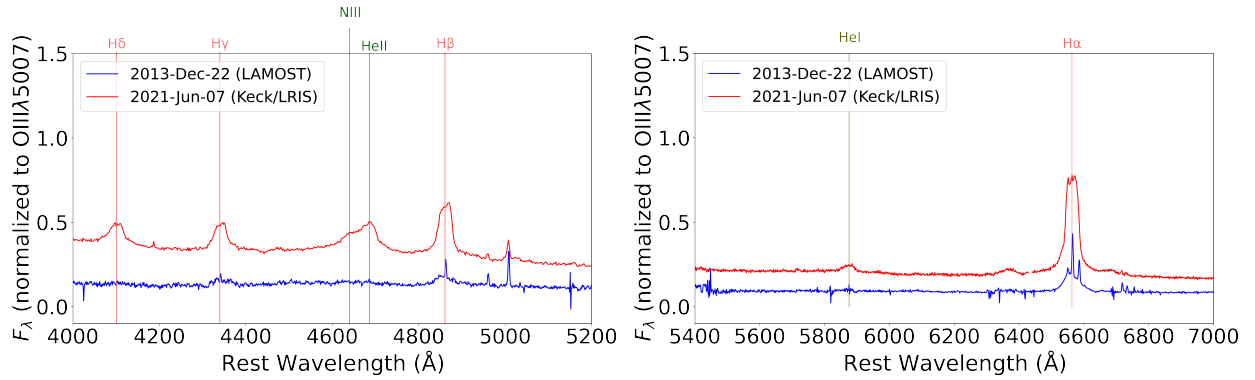


Figure 14. Comparison of the host-subtracted and extinction corrected LAMOST and Keck spectra divided by the $[\text{O III}] \lambda 5007$ flux as found by PYQSOFIT.

APPENDIX

A. NORMALIZED KECK AND LAMOST SPECTRA

Figure 14 shows the archival LAMOST and near-peak (classification) Keck spectra of AT 2021loi, but with flux densities normalized such that the integrated flux of the best-fitting $[\text{O III}] \lambda 5007$ line profile would result in $1 \text{ erg s}^{-1} \text{ cm}^{-2}$. To derive the corresponding normalization factor for each spectrum, we employed the PYQSOFIT spectral fitting procedure (see Section 4.2), but note that in this case we did not try to assign any physical meaning to the continuum decomposition, broad line profiles, or other parameters. As we do not expect the $[\text{O III}] \lambda 5007$ to vary within timescales of a few years (see discussion, and a rare counter-example, in Peterson et al. 2013), these normalized spectra serve to further highlight the differences in continuum and broad line emission between the two epochs, independent of potential seeing and aperture effects.

B. DETAILS REGARDING OPTICAL SPECTRA

Table 4 lists basic details regarding the optical spectra we use and some key spectral measurements, derived through our spectral fitting (see Section 4.2).

Table 4. Optical Spectroscopy of AT 2021loi

MJD	Telescope/Instrument	R^a	$F(\text{H}\beta)$	$F(\text{BF})^b$	$F([\text{O III}] \lambda 5007)$	$\log L_{5100}$	FWHM($\text{H}\beta$)
		(approx.)	($10^{-15} \text{ erg cm}^{-2} \text{ s}^{-1}$)	($10^{-15} \text{ erg cm}^{-2} \text{ s}^{-1}$)	($10^{-15} \text{ erg cm}^{-2} \text{ s}^{-1}$)	(erg s^{-1})	(km s^{-1})
56648.00	LAMOST	1800	10.12 ± 0.54	5.82 ± 0.46	2.29 ± 0.12	42.5	3024 ± 248
59372.61	Keck/LRIS	900	47.12 ± 2.13	55.88 ± 2.96	2.42 ± 0.11	43.48	2146 ± 31
59378.59	Las Cumbres/FLOYDS-N	500	39.41 ± 2.06	35.31 ± 1.85	2.20 ± 0.12	43.59	2087 ± 94
59399.60	Las Cumbres/FLOYDS-N	500	58.42 ± 2.55	40.49 ± 1.76	2.48 ± 0.11	43.65	2092 ± 61
59407.55	Las Cumbres/FLOYDS-N	500	53.16 ± 2.42	25.91 ± 1.18	2.54 ± 0.12	43.51	1917 ± 77
59415.53	Las Cumbres/FLOYDS-N	500	63.08 ± 3.47	29.82 ± 1.64	3.39 ± 0.19	43.53	2162 ± 63
59429.46	Las Cumbres/FLOYDS-N	500	78.90 ± 2.52	31.77 ± 1.02	4.17 ± 0.13	43.65	2051 ± 120
59446.52	Las Cumbres/FLOYDS-N	500	69.93 ± 0.97	22.13 ± 0.31	3.08 ± 0.04	43.48	2078 ± 52
59454.61	Las Cumbres/FLOYDS-N	500	65.78 ± 1.14	21.25 ± 0.37	2.52 ± 0.04	43.44	2125 ± 49
59462.49	Las Cumbres/FLOYDS-N	500	62.87 ± 1.27	19.08 ± 0.38	2.78 ± 0.06	43.41	2184 ± 80
59470.44	Las Cumbres/FLOYDS-N	500	72.48 ± 1.82	21.76 ± 0.55	3.25 ± 0.08	43.43	2171 ± 101
59478.44	Las Cumbres/FLOYDS-N	500	69.84 ± 4.29	22.58 ± 1.39	1.92 ± 0.12	43.25	2279 ± 189
59489.37	Las Cumbres/FLOYDS-N	500	65.38 ± 1.72	23.26 ± 0.61	2.58 ± 0.07	43.29	2409 ± 100
59504.28	Las Cumbres/FLOYDS-N	500	48.26 ± 0.88	12.11 ± 0.22	1.04 ± 0.02	42.99	2272 ± 53
59507.37	Las Cumbres/FLOYDS-N	500	60.37 ± 2.93	15.40 ± 0.75	1.25 ± 0.06	42.63	2761 ± 103
59522.34	Las Cumbres/FLOYDS-N	500	52.01 ± 1.40	17.02 ± 0.46	1.68 ± 0.05	42.95	2440 ± 69
59537.35	Las Cumbres/FLOYDS-N	500	67.34 ± 1.06	19.30 ± 0.30	2.44 ± 0.04	43.18	2370 ± 44
59585.29	Las Cumbres/FLOYDS-N	500	54.20 ± 0.98	17.20 ± 0.31	1.88 ± 0.03	42.69	2365 ± 74
59601.24	Las Cumbres/FLOYDS-N	500	70.13 ± 1.08	19.88 ± 0.31	2.62 ± 0.04	43.11	2340 ± 57
59616.22	Las Cumbres/FLOYDS-N	500	66.00 ± 0.98	17.97 ± 0.27	2.62 ± 0.04	43.0	2265 ± 54
59804.55	Las Cumbres/FLOYDS-N	500	72.00 ± 0.91	24.61 ± 0.31	2.00 ± 0.03	42.46	2312 ± 148
59839.52	Las Cumbres/FLOYDS-N	500	57.93 ± 9.19	8.00 ± 1.27	1.50 ± 0.23	42.63	2333 ± 528

^aThe (approximate) resolving power of the spectrum.

^bWith the term BF here, we mean the double peaked emission feature around $\sim 4680 \text{ \AA}$ originating from $\text{He II } \lambda 4686$ and $\text{N III } \lambda 4640$.